A Unified Theory for the Great Plains Nocturnal Low-Level Jet

ALAN SHAPIRO

School of Meteorology, and Center for Analysis and Prediction of Storms, University of Oklahoma, Norman, Oklahoma

EVGENI FEDOROVICH

School of Meteorology, University of Oklahoma, Norman, Oklahoma

STEFAN RAHIMI

Department of Atmospheric Science, University of Wyoming, Laramie, Wyoming

(Manuscript received 9 October 2015, in final form 22 February 2016)

ABSTRACT

A theory is presented for the Great Plains low-level jet in which the jet emerges in the sloping atmospheric boundary layer as the nocturnal phase of an oscillation arising from diurnal variations in turbulent diffusivity (Blackadar mechanism) and surface buoyancy (Holton mechanism). The governing equations are the equations of motion, mass conservation, and thermal energy for a stably stratified fluid in the Boussinesq approximation. Attention is restricted to remote (far above slope) geostrophic winds that blow along the terrain isoheights (southerly for the Great Plains). Diurnally periodic solutions are obtained analytically with diffusivities that vary as piecewise constant functions of time and slope buoyancies that vary as piecewise linear functions of time. The solution is controlled by 11 parameters: slope angle, Coriolis parameter, free-atmosphere Brunt–Väisälä frequency, free-atmosphere geostrophic wind, radiative damping parameter, day and night diffusivities, maximum and minimum surface buoyancies, and times of maximum surface buoyancy and sunset. The Holton mechanism, by itself, results in relatively weak wind maxima but produces strong jets when paired with the Blackadar mechanism. Jets with both Blackadar and Holton mechanisms operating are shown to be broadly consistent with observations and climatological analyses. Jets strengthen with increasing geostrophic wind, maximum surface buoyancy, and day-to-night ratio of the diffusivities and weaken with increasing Brunt–Väisälä frequency and magnitude of minimum slope buoyancy (greater nighttime cooling). Peak winds are maximized for slope angles characteristic of the Great Plains.

1. Introduction

The nocturnal low-level jet (LLJ) is a low-level maximum in the boundary layer wind profile common to the Great Plains of the United States (Bonner 1968; Mitchell et al. 1995; Stensrud 1996; Whiteman et al. 1997; Arritt et al. 1997; Song et al. 2005; Walters et al. 2008) and other places worldwide (Sládkovič and Kanter 1977; Stensrud 1996; Beyrich et al. 1997; Rife et al. 2010; Fiedler et al. 2013). Typically LLJs begin to develop around sunset in fair weather conditions, reach peak intensity a few hours after midnight, and dissipate with the onset of daytime convective mixing. Peak LLJ winds are generally supergeostrophic, with wind vectors that turn anticyclonically through the night. Data from Doppler sodars, lidars, and other high-resolution observational platforms indicate that peak LLJ winds are often found within 500 m of the ground (Whiteman et al. 1997; Banta et al. 2002; Banta 2008; Song et al. 2005; Conangla and Cuxart 2006; Baas et al. 2009; Werth et al. 2011; Kallistratova and Kouznetsov 2012; Hu et al. 2013; Klein et al. 2014). Early analyses of pibal and rawinsonde data over the Great Plains of the United States revealed that LLJs in that region can be hundreds of kilometers wide (Means 1954; Hoecker 1963; Bonner 1968; Bonner et al. 1968) and up to 1000 km long (Bonner 1968; Bonner et al. 1968). The maximum winds in the majority of Great Plains LLJs are southerly; the

Corresponding author address: Alan Shapiro, School of Meteorology, University of Oklahoma, 120 David L. Boren Blvd., Room 5900, Norman, OK 73072.
E-mail: ashapiro@ou.edu

DOI: 10.1175/JAS-D-15-0307.1

southerly jets occur roughly twice as often in the warm season as in the cold season (Bonner 1968; Whiteman et al. 1997; Song et al. 2005; Walters et al. 2008). In Bonner's (1968) 2-yr climatological analysis, Great Plains LLJs occurred most frequently over Kansas and Oklahoma in a corridor roughly straddling the 98°W meridian. However, there is much interannual variability in the jet characteristics (Song et al. 2005; Walters et al. 2008), and the peak frequency from a longer-term (40 yr) analysis (Walters et al. 2008) was located farther south than in the Bonner (1968) study, in southern and southwestern Texas.

LLJs have significant economic and public health and safety impacts. LLJs promote deep convection and beneficial (as well as hazardous) heavy rain events through moisture transport and lifting (Means 1954; Pitchford and London 1962; Maddox 1980, 1983; Cotton et al. 1989; Stensrud 1996; Higgins et al. 1997; Arritt et al. 1997; Trier et al. 2006, 2014; French and Parker 2010). They transport pollutants hundreds of miles over the course of a night and mix elevated pollutants down to the surface (Zunckel et al. 1996; Banta et al. 1998; Solomon et al. 2000; Mao and Talbot 2004; Darby et al. 2006; Bao et al. 2008; Klein et al. 2014; Delgado et al. 2014). They also transport fungi, pollen, spores, and insects, including allergens, agricultural pests, and plant and animal pathogens (Drake and Farrow 1988; Wolf et al. 1990; Westbrook and Isard 1999; Isard and Gage 2001; Zhu et al. 2006; Westbrook 2008). LLJs are an important wind resource for the wind energy industry (Cosack et al. 2007; Storm et al. 2009; Emeis 2013, 2014; Banta et al. 2013).

There is considerable interest in characterizing and improving the representation of LLJs in numerical weather prediction. Storm et al. (2009) found that the Weather Research and Forecasting (WRF) Model run with a variety of boundary layer and radiation parameterizations underestimated LLJ strength and overestimated LLJ height in two southern Great Plains test cases. Steeneveld et al. (2008) reported similar difficulties in experiments with three regional models. Werth et al. (2011) found that the life cycles of southern Great Plains LLJs were generally well predicted using a regional model but that the modeled jets were again placed too high. Mirocha et al. (2016) found large discrepancies between lidar observations and WRF Model predictions of near-surface winds in northern Great Plains LLJs. Increasing the model spatial resolution did little to improve the wind speed forecasts and sometimes even degraded the results. In a comparison of wind profiles from the North American Regional Reanalysis (NARR) and rawinsonde observations, Walters et al. (2014) noted that the NARR underestimated LLJ frequencies and urged caution in the use of NARR LLJ winds in LLJ case studies and numerical model validations. The problems identified in some of these studies were attributed, in part, to deficiencies in parameterizations of turbulent exchange in the nocturnal stable boundary layer. Indeed, understanding and modeling boundary layers under stably stratified conditions is notoriously difficult (Mahrt 1998, 1999; Derbyshire 1999; Mironov and Fedorovich 2010; Fernando and Weil 2010; Holtslag et al. 2013; Sandu et al. 2013; Steeneveld 2014).

In addition to the current poor state of knowledge of nocturnal stable boundary layers, there are also remaining uncertainties in understanding the physical mechanisms of the development of Great Plains LLJs. We now discuss the main theories underpinning this phenomenon.

Concerning the geographical preference of the Great Plains LLJ, Wexler (1961) proposed that the strong southerly time-mean current originates from blocking of easterly trade winds by the Rocky Mountains in a manner similar to the westward intensification of oceanic currents along eastern seaboards. Terrain versus no-terrain experiments performed in a regional model (Pan et al. 2004) and a general circulation model (Ting and Wang 2006; Jiang et al. 2007) suggested that topography is essential for maintaining a strong southerly time-mean flow over the Great Plains during the summer. However, Parish and Oolman (2010) found that the strong southerly mean flow over the Great Plains in their nonhydrostatic mesoscale simulations of summertime LLJs originates from the mean heating of the gentle slope of the Great Plains rather than from mechanical blocking by the Rocky Mountains.

Blackadar (1957, hereafter B57) and Buajitti and Blackadar (1957, hereafter BB57) described the LLJ as an inertial oscillation (IO) in the atmospheric boundary layer resulting from the sudden disruption of the Ekman balance near sunset when turbulent (frictional) stresses are rapidly shut down.[1] The IO-theory predictions of low-altitude winds that turn anticyclonically during the night and reach peak intensity in the early morning have been amply verified in the literature. However, the B57 IO theory cannot explain how the peak winds in some LLJs exceed the geostrophic values by more than 100%.[2] Additionally, B57 proposed a close association between

[1] Inviscid IOs were described in B57. IOs with frictional effects were considered in BB57 and subsequent studies (Sheih 1972; Thorpe and Guymer 1977; Singh et al. 1993; Tan and Farahani 1998; Shapiro and Fedorovich 2010; Van de Wiel et al. 2010). These IO studies did not make provision for a diurnally heated/cooled slope and did not include a thermal energy equation.

[2] The 100% limit is itself an overestimate for real IOs since it pertains to surface winds that satisfy the no-slip condition in the late afternoon but are then freed of the frictional constraint after sunset. For real flows, friction is inevitably important near the surface.

the height of the wind maximum and the top of the nocturnal surface inversion layer. While there are some confirmations of such an association (B57; Coulter 1981; Baas et al. 2009; Werth et al. 2011; Kallistratova and Kouznetsov 2012), the many studies where this association was not found (Hoecker 1963; Bonner 1968; Mahrt et al. 1979; Brook 1985; Whiteman et al. 1997; Andreas et al. 2000; Milionis and Davies 2002) suggest that such a link may not be straightforward.

Holton (1967, hereafter H67) studied the response of the atmosphere to a diurnally heated/cooled slope without provision for a time dependence in the turbulent friction (i.e., without the B57–BB57 frictional relaxation). The analysis was restricted to cases where the free-atmosphere geostrophic wind flowed parallel to terrain isoheights. The governing equations were the one-dimensional (1D; in slope-normal coordinate) Boussinesq equations of motion and thermal energy equation for a viscous stably stratified fluid. The H67 solutions described baroclinically generated wind oscillations in the atmospheric boundary layer, but the phase of the oscillations was not captured correctly, and the wind profiles were not as jetlike as in observed LLJs.

Although neither the H67 slope theory nor the B57–BB57 IO theory is generally sufficient to explain observations of Great Plains LLJs, the physical mechanisms underlying these theories are plausible, and it has long been speculated that both can be important in the development of Great Plains LLJs. The question of dominant mechanism is not without some controversy, however. For instance, on the basis of two-dimensional numerical modeling of the boundary layer diurnal cycle over gently sloping terrain, McNider and Pielke (1981) and Savijärvi (1991) reach opposite conclusions. A slope effect plays "a dominant role in the evolution of the diurnal wind structure" in the former study but "has only a small guiding effect" in the latter study. These disparate conclusions may be an outcome of seasonal differences: Savijärvi (1991) used composite data from 21 cases in March–June 1967, while McNider and Pielke (1981) used data typical of midsummer. The diurnal range of the surface geostrophic wind (representing thermal forcing of the slope) was 2.5 times larger in the latter study, while the free-atmosphere geostrophic wind was 1.6 times larger in the former study. In an analysis of general circulation model output, Jiang et al. (2007) concluded that both the IO and buoyancy-associated slope flow mechanisms were equally important in establishing the phase and amplitude of the modeled LLJs. Based on results from a mesoscale numerical model and an idealized inviscid analysis, Parish and Oolman (2010) concluded that the nocturnal wind maxima in their summertime Great Plains LLJs resulted from inertial oscillations arising from frictional decoupling. However, they also found that diabatic heating of the slope strengthened the late-afternoon low-level geostrophic wind—a background field on which the frictional decoupling acted—which then intensified the nocturnal wind maximum.

Early studies that sought to combine the H67 and B57–BB57 mechanisms into a single framework considered the 1D (in true vertical coordinates) equations of motion but did not make provision for a thermal energy equation [Bonner and Paegle (1970) and references therein]. Rather, a diurnally warming/cooling atmospheric boundary layer was explicitly specified by imposing a corresponding geostrophic wind profile.[3] The eddy viscosity and geostrophic wind were specified as sums of time-mean and diurnally varying components, with the diurnally varying part of the geostrophic wind decreasing exponentially with height. When appropriately tuned, the Bonner and Paegle (1970) model [and its extension by Paegle and Rasch (1973)] produced results that were in reasonable agreement with observations. More recently, Du and Rotunno (2014) simplified the Bonner and Paegle (1970) model by setting the stress-divergence term proportional to the velocity vector, resulting in a zero-dimensional (no height dependence) model. Such a model cannot predict the vertical structure of a jet but can be used to estimate jet strength and timing. The amplitude and phase of the modeled LLJs were in good agreement with NARR data, particularly when NARR-derived latitudinal variations in the amplitudes of the mean and diurnally varying components of the pressure gradient force were specified.

Shapiro and Fedorovich (2009) treated the combined H67 and B57/BB57 problem as an inviscid postsunset initial-value problem, essentially generalizing the B57 formulation to include a thermal energy equation for a stably stratified fluid overlying the sloping Great Plains. The wind and buoyancy variables were specified through initial (sunset) conditions, and the subsequent motion was an inertia–gravity oscillation. Stronger initial buoyancies played an analogous role in strengthening the LLJ as stronger initial ageostrophic winds did in the IO theory. The initial buoyancy was obtained in terms of slope angle, free-atmosphere stratification, distance beneath the capping inversion, and parameters characterizing the

[3] Thermal effects in the sloping atmospheric boundary layer were described in terms of buoyancy in H67 and in terms of geostrophic wind (east–west pressure gradient) or thermal wind in Bonner and Paegle (1970), Paegle and Rasch (1973), Parish and Oolman (2010), and Du and Rotunno (2014). The relations between buoyancy, geostrophic wind, and thermal wind in our Boussinesq model are given in appendix A.

residual layer and capping inversion. The free-atmosphere stratification played a dual role: it attenuated the upslope and downslope motions (as had been noted by H67 and others) but was also associated with increased initial buoyancy, which tended to increase the oscillation amplitude.

In this study, we present a unified theory for the Great Plains LLJ in which the jet appears in the nighttime phase of oscillations arising from diurnal cycles of turbulent mixing (Blackadar mechanism) and heating/cooling of the slope (Holton mechanism). As in H67, the equations of motion are supplemented with a thermal energy equation. The buoyancy evolves in accord with the coupled governing equations, unlike the thermal field proxy (geostrophic wind or equivalent) in Bonner and Paegle (1970), Paegle and Rasch (1973), Parish and Oolman (2010), and Du and Rotunno (2014), which is specified.

In section 2, we formulate our problem and show how a special linear transformation simplifies the governing equations. An analytical solution for periodic motions is derived in section 3. The case where the diffusivities vary as piecewise constant functions of time and the surface buoyancy varies as a piecewise linear function of time is explored in section 4. A summary follows in section 5.

2. Problem formulation and governing equations

An inclined planar surface (slope) is subjected to a diurnally periodic but spatially uniform thermal forcing. Far above the slope, a spatially and temporally uniform pressure gradient drives a geostrophic wind that blows parallel to the terrain isoheights (as in H67). For a Great Plains analysis, this free-atmosphere geostrophic wind is considered southerly. As in H67, Parish and Oolman (2010), and Du and Rotunno (2014), the model variables are independent of the cross-slope coordinate. We parameterize the turbulent transfer of heat and momentum using an eddy viscosity approach in which the diffusivities are diurnally periodic. Attention is restricted to periodic flows; transients associated with any particular initial state are not investigated.

We work with a slope-following right-handed Cartesian coordinate system (Fig. 1) with x axis pointing downslope, y axis pointing across the slope, and z axis directed perpendicular to the slope. The slope is inclined at an angle α to the true horizontal coordinate x^*. For a Great Plains analysis, the x^* axis points eastward (higher terrain toward the west). The true vertical coordinate (normal to x^*) is denoted by z^*. The unit vectors in the x, x^*, z, and z^* directions are denoted by $\mathbf{i}$, $\mathbf{i}^*$, $\mathbf{k}$, and $\mathbf{k}^*$, respectively.

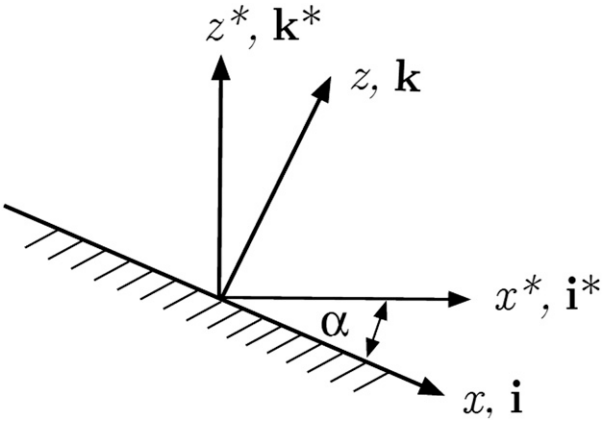

FIG. 1. Slope-following coordinate system. The downslope (x) and slope-normal (z) coordinates are inclined at an angle α to the horizontal (x^*) and vertical (z^*) coordinates, respectively. The motion is independent of the cross-slope (y; into page) coordinate.

a. Governing equations

The governing equations are the equations of motion, mass conservation, and thermal energy under the Boussinesq approximation. Given the along-slope homogeneity of the forcings, the x- and y-velocity components (u and v, respectively) are constant on x–y planes, and the mass conservation equation (incompressibility condition) together with the impermeability condition imply that the slope-normal (z) velocity component w is identically zero. The remaining governing equations[4] can then be written as

$$\frac{\partial u}{\partial t} = fv - \frac{\partial \Pi}{\partial x} - b\sin\alpha + K\frac{\partial^2 u}{\partial z^2}, \tag{2.1}$$

$$\frac{\partial v}{\partial t} = -fu + K\frac{\partial^2 v}{\partial z^2}, \tag{2.2}$$

$$0 = -\frac{\partial \Pi}{\partial z} + b\cos\alpha, \quad \text{and} \tag{2.3}$$

$$\frac{\partial b}{\partial t} = uN^2\sin\alpha - \delta b + K\frac{\partial^2 b}{\partial z^2}, \tag{2.4}$$

where (2.1) and (2.2) are the downslope and cross-slope equations of motion, respectively, (2.3) is the quasi-hydrostatic equation (Mahrt 1982), and (2.4) is the thermal energy equation. Here, $\Pi \equiv [p - P(z^*)]/\rho_0$ is a kinematic pressure perturbation, $b \equiv g[\theta - \theta_e(z^*)]/\theta_0$ is buoyancy, p is pressure, θ is potential temperature, $\theta_e(z^*)$ is the potential temperature in the free atmosphere, $N \equiv \sqrt{(g/\theta_0)d\theta_e/dz^*}$ is the free-atmosphere Brunt–Väisälä

[4] If the x axis is pointed upslope instead of downslope, the signs of the $\sin\alpha$ terms in these equations should be reversed.

frequency (considered constant), and a subscript "0" denotes a constant reference value of the corresponding thermodynamic variable. The quantity $P(z^*) \equiv p_e(z^*, x_0^*)$ is the pressure profile in the free atmosphere at a prescribed location x_0^* Since $\partial P/\partial x^* = 0$, the free-atmosphere geostrophic balance must be supported by Π rather than by P. For simplicity, we refer to $f \equiv 2\boldsymbol{\Omega} \cdot \mathbf{k}$ ($\boldsymbol{\Omega}$ is the angular velocity of Earth's rotation) as the Coriolis parameter since its value differs insignificantly from that of the true Coriolis parameter $f^* \equiv 2\boldsymbol{\Omega} \cdot \mathbf{k}^*$ on the Great Plains, where the angle between $\mathbf{k}$ and $\mathbf{k}^*$ is ~0.1°. We treat f as constant.

Equations (2.1)–(2.4) comprise a nearly exact set of governing equations for 1D Boussinesq flow, with most of the missing terms vanishing identically because of spatial homogeneity (in x) rather than being neglected. For instance, the momentum advection terms in the three equations of motion are identically zero. The only thermal advection term to survive in (2.4) is the advection of the free-atmosphere potential temperature by the true vertical (z^*) velocity component (which is $-u \sin\alpha$). All x-derivative diffusion terms vanish in (2.1), (2.2), and (2.4)

As in the katabatic wind studies of Egger (1985) and Mo (2013), we include a radiative damping (Newtonian heating/cooling) term $-\delta b$ in the thermal energy equation, with the damping parameter δ held constant. The reciprocal parameter δ^{-1} is the damping time scale. A radiative damping term was also included in H67 but was based on the difference between temperature and a specified diurnally varying radiative equilibrium temperature.

As in H67, the turbulent heat and momentum exchanges are parameterized through height-invariant turbulent diffusion coefficients (diffusivities) $K > 0$, considered equal for momentum and heat (i.e., the turbulent Prandtl number is unity). However, while H67 also took K to be temporally constant, our K is diurnally periodic. Bonner and Paegle (1970) also took their turbulent momentum exchange coefficient to be diurnally periodic and height invariant.

It can be noted that estimated $K(z)$ profiles in Ekman layers typically vary slowly in height and attain a local maximum at low or midlevels of the boundary layer (O'Brien 1970; Stull 1988; Grisogono 1995; Jeričević and Večenaj 2009). Steady-state solutions of the Ekman equations associated with such K have been obtained analytically by Brown (1974), Nieuwstadt (1983), Miles (1994), Grisogono (1995), Tan (2001), and others. In contrast, in stable boundary layers featuring a pronounced low-level wind maximum, as in nocturnal low-level jets or katabatic flows, height variations in K are of finer scale, and $K(z)$ can exhibit multiple extrema (McNider and Pielke 1981; Cuxart and Jiménez 2007; Axelsen and van Dop 2009). The shape of K profiles in sloping boundary layers with jets therefore varies considerably over a diurnal cycle. Such K are nonseparable functions of z and t, which render the governing equations insoluble by traditional analytical methods. Accordingly, for analytical tractability, we proceed with height-invariant K. Reasonable results obtained with this simplified approach might suggest that it is more important to account for the rapid and drastic temporal changes of K attending the early evening and morning transitions than to account for the vertical variations of K.

We have chosen a turbulent Prandtl number of unity primarily for mathematical expediency: it is the only choice for which the governing equations reduce to the simpler forms derived in section 2b. However, Wilson (2012) obtained qualitatively reasonable eddy viscosity model simulations of day 33 of the Wangara experiment using that value. A value of unity is also consistent with estimates reported in stable conditions (nighttime phase of our analysis). For weakly stable conditions, Howell and Sun (1999) show Prandtl numbers scattered around unity, with no strong dependence on the stability parameter, while Schumann and Gerz (1995) estimate Prandtl numbers between 0.8 and 1.2. Cuxart and Jiménez's (2007) estimates of the Prandtl number in their nocturnal LLJ LES using the Stable Atmospheric Boundary Layer Experiment in Spain-1998 (SABLES-98) data are generally between 0.8 and 1. However, under unstable conditions (daytime phase of our analysis), Prandtl numbers in the surface layer are generally smaller than 1—about 0.3–0.4 for strongly unstable regimes (Businger et al. 1971; Gibson and Launder 1978; results in those studies shown for the inverse Prandtl number)—suggesting that during the day our analysis likely underestimates the mixing of heat relative to momentum at low levels. Prandtl numbers are generally not reported for the mixed layer because of measurement difficulties and the large uncertainty in estimates of vertical gradients of wind and temperature when these gradients are small.

On the slope we impose the no-slip conditions

$$u(0,t) = 0, \quad v(0,t) = 0, \tag{2.5}$$

and specify the surface buoyancy

$$b(0,t) = b_s(t), \tag{2.6}$$

where $b_s(t)$ is diurnally periodic. Far above the slope ($z \to \infty$) we take $b \to 0$, in which case (2.4) indicates that u must also vanish. Thus, the wind far above the slope

blows parallel to the topographic height contours. In view of (2.1), this remote wind is in a geostrophic balance. These remote conditions can be written as

$$\lim_{z\to\infty} v = v_G \neq 0, \quad \lim_{z\to\infty} u = 0, \quad \lim_{z\to\infty} b = 0, \quad \text{and} \tag{2.7a}$$

$$\lim_{z\to\infty} \frac{\partial \Pi}{\partial x} = f v_G . \tag{2.7b}$$

For brevity, we refer to v_G as the geostrophic wind even though it actually is the geostrophic wind far above the slope (i.e., free-atmosphere geostrophic wind).

Since b is independent of x, taking $\partial/\partial x$ of (2.3) yields $\partial^2\Pi/\partial x\partial z = 0$, the z-integral of which is $\partial\Pi/\partial x = F(x, t)$, where the function of integration F is, at most, a function of x and t. In view of (2.7b), $F(x, t) = fv_G$. Since v_G is constant, F is constant. Thus, the along-slope perturbation pressure gradient $\partial\Pi/\partial x$ is spatially and temporally constant; it is imposed on the boundary layer from aloft.

In terms of the ageostrophic wind components $v_a \equiv v - v_G$ and u (which is ageostrophic since the x-component geostrophic wind is zero), (2.1) and (2.2) become

$$\frac{\partial u}{\partial t} = f v_a - b\sin\alpha + K\frac{\partial^2 u}{\partial z^2} \quad \text{and} \tag{2.8}$$

$$\frac{\partial v_a}{\partial t} = -fu + K\frac{\partial^2 v_a}{\partial z^2}, \tag{2.9}$$

with $\lim_{z\to\infty} v_a = 0$. Equations (2.4), (2.8), and (2.9) comprise a closed system. Equation (2.3) was used to establish constancy of the along-slope pressure gradient throughout the boundary layer but is now no longer needed. It can be seen from (2.8) that positive buoyancy plays an analogous role in forcing upslope flow as a negative ageostrophic wind. During the late afternoon, at the low levels where the LLJ will eventually develop, the buoyancy is positive and the wind is subgeostrophic, implying that the ageostrophic wind is northerly (i.e., negative). The effects of buoyancy and ageostrophic wind during the early evening transition are thus additive and set the stage for the initiation of a stronger inertia–gravity oscillation. This joint effect is described more fully in Shapiro and Fedorovich (2009).

Although our analysis is restricted to constant values of the remote geostrophic wind v_G, a time-dependent $v_G(t)$ function would not violate the 1D model restriction and could, in principle, be incorporated into a revised analysis. Had we made provision for such a function, (2.9) would include an inhomogeneous term $\partial v_G/\partial t$. The two equations for Q derived in the next section would then also be inhomogeneous.

b. Uncoupling the governing equations

Although our governing equations can be cast as a single sixth-order partial differential equation (as in H67), a special linear transformation can be found that reduces the governing equations to two much simpler equations. Our approach parallels Gutman and Malbakhov's (1964) analysis for 1D katabatic flows but is more involved in the present case because of our inclusion of a radiative damping term.

Taking $\sin\alpha \times$ (2.4) + $k \times$ (2.8) + $l \times$ (2.9), where k and l are constants, produces

$$\frac{\partial Q}{\partial t} = kfv_a - b\sin\alpha(k+\delta) + u(N^2\sin^2\alpha - lf) + K\frac{\partial^2 Q}{\partial z^2}, \tag{2.10}$$

where $Q \equiv b\sin\alpha + ku + lv_a$. We seek k and l such that the sum of the undifferentiated terms in (2.10) is proportional to Q ($=\mu Q$, where μ is a constant of proportionality). In other words, if k and l (and μ) are chosen such that

$$kfv_a - b\sin\alpha(k+\delta) + u(N^2\sin^2\alpha - lf) = \mu Q, \tag{2.11}$$

then (2.10) reduces to $\partial Q/\partial t = \mu Q + K\partial^2 Q/\partial z^2$. If $\mu \neq 0$ then (2.11) is satisfied by

$$\mu = -k - \delta, \quad l = kf/\mu, \quad k = (N^2\sin^2\alpha - lf)/\mu. \tag{2.12}$$

Eliminating l and μ from (2.12) in favor of k yields the cubic equation

$$k^3 + 2\delta k^2 + (\omega^2 + \delta^2)k + \delta N^2\sin^2\alpha = 0, \tag{2.13}$$

where $\omega^2 \equiv f^2 + N^2\sin^2\alpha$.

Equation (2.13) is solved in appendix B. One root (k_1) is real, and two roots (k_2 and k_3) form a complex conjugate pair: that is, $k_3 = k_2^*$, where the asterisk denotes complex conjugation. Corresponding to k_1 are real values of μ and l from (2.12), labeled μ_1 and l_1. The associated Q is

$$Q_1 = b\sin\alpha + k_1 u + l_1 v_a . \tag{2.14}$$

For $k = k_2$, (2.12) yields generally complex μ_2 and l_2, and we obtain a complex Q with the real and imaginary parts, respectively:

$$\Re(Q_2) = b\sin\alpha + \Re(k_2)u + \Re(l_2)v_a \quad \text{and} \tag{2.15}$$

$$\Im(Q_2) = \Im(k_2)u + \Im(l_2)v_a . \tag{2.16}$$

Since u, v, and b are completely specified by Q_1 and Q_2 (shown below), it suffices to work with Q_1 and Q_2 (equivalently, we could work with Q_1 and $Q_3 = Q_2^*$). The

governing equations thus reduce to the two uncoupled parabolic equations

$$\frac{\partial Q_j}{\partial t} = \mu_j Q_j + K\frac{\partial^2 Q_j}{\partial z^2}, \quad j = 1,2 \tag{2.17}$$

subject to boundary conditions based on (2.5), (2.6) and (2.7a):

$$Q_j(0,t) = b_s(t)\sin\alpha - l_j v_G, \quad j = 1,2 \quad \text{and} \tag{2.18a}$$

$$\lim_{z\to\infty} Q_j = 0, \quad j = 1,2. \tag{2.18b}$$

Inverting (2.14)–(2.16) yields expressions for u, v, and b in terms of Q_1 and Q_2:

$$u = -\frac{\Im(l_2)}{D}Q_1 + \frac{\Im(l_2)}{D}\Re(Q_2) + \frac{l_1 - \Re(l_2)}{D}\Im(Q_2), \tag{2.19}$$

$$v_a = \frac{\Im(k_2)}{D}Q_1 - \frac{\Im(k_2)}{D}\Re(Q_2) - \frac{k_1 - \Re(k_2)}{D}\Im(Q_2), \tag{2.20}$$

and

$$\begin{aligned} b = {} & \frac{\Re(k_2)\Im(l_2) - \Im(k_2)\Re(l_2)}{D\sin\alpha}Q_1 \\ & + \frac{l_1\Im(k_2) - k_1\Im(l_2)}{D\sin\alpha}\Re(Q_2) \\ & + \frac{k_1\Re(l_2) - l_1\Re(k_2)}{D\sin\alpha}\Im(Q_2), \end{aligned} \tag{2.21}$$

where

$$D \equiv \Im(k_2)[l_1 - \Re(l_2)] - \Im(l_2)[k_1 - \Re(k_2)] \tag{2.22}$$

In the next section, we obtain periodic solutions for Q_1 and Q_2.

3. Periodic solutions

We seek diurnally periodic solutions for Q_j over a 24-h interval from sunrise, at $t = 0$, until the next sunrise, at $t = t_{24} = 24$ h. Periodicity is achieved by setting

$$Q_j(z,0) = Q_j(z,t_{24}), \quad j = 1,2. \tag{3.1}$$

The solution for $t > t_{24}$ can be obtained from the 24-h solution through the relation $Q(z, \tau + Mt_{24}) = Q(z, \tau)$, where $\tau \equiv t - Mt_{24} < t_{24}$, and M is the day number.

a. *Nonexistence of periodic solutions for $\delta = 0$*

If there is no radiative damping ($\delta = 0$), then (B7) yields $k_1 = 0$, and (2.13) yields $\mu_1 = 0$, which violates the prerequisite condition for (2.13). We must therefore revisit the $j = 1$ case (though there is no such difficulty for $j = 2$). Setting $k_1 = 0$ and $l_1 = N^2\sin^2\alpha/f$ reduces (2.10) to the diffusion equation

$$\frac{\partial Q_1}{\partial t} = K\frac{\partial^2 Q_1}{\partial z^2} \tag{3.2}$$

for $Q_1 \equiv b\sin\alpha + v_a N^2\sin^2\alpha/f$. This is essentially one of the two uncoupled equations obtained by Gutman and Malbakhov (1964). The boundary conditions for Q_1 are

$$Q_1(0,t) = b_s\sin\alpha - \frac{N^2\sin\alpha}{f}v_G \quad \text{and} \tag{3.3}$$

$$\lim_{z\to\infty} Q_1 = 0. \tag{3.4}$$

Averaging (3.2) over the 24-h interval and using (3.1) yields

$$\frac{d^2(\overline{KQ_1})}{dz^2} = 0, \tag{3.5}$$

where an overbar denotes a 24-h average. Equation (3.5) integrates to

$$\overline{KQ_1} = A + Bz, \tag{3.6}$$

where A and B are constants. In view of (3.4), $A = B = 0$, and so $\overline{KQ_1} = 0$ for all z. However, since $\overline{KQ_1}$ is specified at $z = 0$ through $K(t)$ and $Q_1(0, t)$ [the latter specified via (3.3) through choices for α, N, f, v_G, and $b_s(t)$], $\overline{KQ_1}$ only vanishes at $z = 0$ for particular (artificial) arrangements of the governing parameters. Alternatively, if A is chosen so that (3.3) is satisfied, then (3.4) is violated. We conclude that diurnally periodic solutions are not possible for arbitrary governing parameters.

To shed light on this result, consider a simple initial value problem consisting of (3.2) with temporally constant K, $v_G = 0$, initial state $Q_1(z, 0) = 0$, remote condition $\lim_{z\to\infty} Q_1(z, t) = 0$, and a surface buoyancy that is suddenly imposed at $t = 0$ and thereafter maintained such that $Q_1(0, t)$ is a nonzero constant for $t > 0$. This problem is equivalent to 1D heat conduction in a semi-infinite solid whose boundary is suddenly subjected to a constant temperature perturbation. The analytical solution (Carslaw and Jaeger 1959; Shapiro and Fedorovich 2013), describes the continual vertical growth of a thermal boundary layer. The layer depth becomes infinite as $t \to \infty$. Similar behavior is found in 1D katabatic flows with provision for the Coriolis force but without radiative damping (Gutman and Malbakhov 1964; Lykosov and Gutman 1972; Egger 1985; Stiperski et al. 2007; Shapiro and Fedorovich 2008) and in 1D models of oceanic flows over sloping seabeds (Garrett 1991; MacCready and Rhines 1991, 1993; Garrett et al.

1993). We speculate that the tendency of the 1D boundary layer to deepen is also a feature of the differential equations for our low-level jet problem (with $\delta = 0$); any tendency of the solutions to oscillate would be conflated with an inexorable deepening of the boundary layer, at least for the buoyancy and cross-slope-flow variables.

b. Periodic solutions for $\delta \neq 0$

In the 1D katabatic flow problem considered by Egger (1985), provision for radiative damping led to steady-state solutions that satisfied both the surface and remote conditions; continual slope-normal growth of thermal and cross-slope momentum boundary layers no longer occurred. The H67 equations also included a radiative damping term and did admit periodic solutions. We anticipate that this will also be the case for our analysis.

We seek the solution of (2.17) using separation of variables. With Q_j in the form

$$Q_j(z,t) = Z_j(z)T_j(t), \tag{3.7}$$

(2.17) becomes

$$\frac{1}{T_j}\frac{dT_j}{dt} = \mu_j + \frac{K(t)}{Z_j}\frac{d^2Z_j}{dz^2}, \tag{3.8}$$

from which follow

$$\frac{dT_j}{dt} = [\mu_j - \lambda_j K(t)]T_j \quad \text{and} \tag{3.9}$$

$$\frac{d^2Z_j}{dz^2} + \lambda_j Z_j = 0, \tag{3.10}$$

where λ_j is a constant. The general solutions of (3.9) and (3.10) are

$$Z_j = A_j \exp(iz\sqrt{\lambda_j}) + B_j \exp(-iz\sqrt{\lambda_j}) \quad \text{and} \tag{3.11}$$

$$T_j = C_j \exp\left(\mu_j t - \lambda_j \int_0^t K(t')\,dt'\right), \tag{3.12}$$

where A_j, B_j, and C_j are constants. To satisfy (2.18b), A_j or B_j must be zero, and we can write

$$Q_j = \text{const} \times \exp\left[\pm iz\sqrt{\lambda_j} + \mu_j t - \lambda_j \int_0^t K(t')\,dt'\right], \tag{3.13}$$

where the plus-or-minus sign choice ensures satisfaction of (2.18b).

Applying the periodicity condition $T(0) = T(t_{24})$ in (3.12) yields

$$1 = \exp[t_{24}(\mu_j - \lambda_j \overline{K})], \tag{3.14}$$

where

$$\overline{K} \equiv \frac{1}{t_{24}}\int_0^{t_{24}} K(t')\,dt'. \tag{3.15}$$

Writing the left-hand side of (3.14) as $1 = \exp(2m\pi i)$, where m is an integer, we find that $t_{24}(\mu_j - \lambda_j\overline{K}) = 2m\pi i$ and thus obtain a distinct λ_j for each m:

$$\lambda_{j,m} = \frac{\mu_j - 2m\pi i/t_{24}}{\overline{K}}. \tag{3.16}$$

The solution (3.13), generalized to include summation over m, appears as

$$Q_j = \exp\{\mu_j[t - \kappa(t)]\}\sum_{m=-\infty}^{\infty} D_{j,m}F_m(t)\exp(\pm iz\sqrt{\lambda_{j,m}}); \tag{3.17}$$

$$F_m(t) \equiv \exp[2m\pi i\kappa(t)/t_{24}]; \tag{3.18}$$

$$\kappa(t) \equiv \frac{1}{\overline{K}}\int_0^t K(t')\,dt'. \tag{3.19}$$

Last, we determine $D_{j,m}$ so that the slope conditions (2.18a) are satisfied. Unfortunately, since K is a function of time, a standard Fourier series approach will not lead to explicit formulas for $D_{j,m}$. Instead, we must derive orthogonality relations for the F_m functions. Toward that end, we consider the time derivatives of (3.18):

$$\frac{dF_m}{dt} = \frac{2m\pi i K(t)}{t_{24}\overline{K}}F_m; \tag{3.20a}$$

$$\frac{dF_n^*}{dt} = -\frac{2n\pi i K(t)}{t_{24}\overline{K}}F_n^*. \tag{3.20b}$$

Adding $F_n^* \times$ (3.20a) to $F_m \times$ (3.20b) leads to

$$\frac{d}{dt}(F_m F_n^*) = \frac{2(m-n)\pi i}{t_{24}\overline{K}}K(t)F_m F_n^*, \tag{3.21}$$

which integrates over the 24-h interval to $(m-n)\int_0^{t_{24}} K(t')F_m(t')F_n^*(t')\,dt' = 0$. For $m \neq n$, the integral must vanish, and therefore F_m and F_n^* are orthogonal over the 24-h interval with respect to the weighting function $K(t)$. For $m = n$, the integral is evaluated as $t_{24}\overline{K}$. We thus obtain the orthogonality relations

$$\int_0^{t_{24}} K(t')F_m(t')F_n^*(t')\,dt' = \delta_{mn}t_{24}\overline{K}, \tag{3.22}$$

where δ_{mn} is the Kronecker delta. The solution procedure now parallels the usual Fourier approach. Applying (2.18a) for Q_j in (3.17) leads to

$$\sum_{m=-\infty}^{\infty} D_{j,m}F_m = [b_s(t)\sin\alpha - l_j v_G]\exp\{-\mu_j[t-\kappa(t)]\}. \tag{3.23}$$

Multiplying (3.23) by $K(t)F_n^*(t)$, integrating the resulting equation over the 24-h interval, and making use of (3.22) and (3.18), yields

$$D_{j,m} = \frac{1}{t_{24}\overline{K}}\int_0^{t_{24}} K(t')[b_s(t')\sin\alpha - l_j v_G]\exp[-\mu_j t' + (\mu_j - 2m\pi i/t_{24})\kappa(t')]\,dt'. \tag{3.24}$$

4. Examples: Piecewise constant $K(t)$, piecewise linear $b_s(t)$

a. Analytical solution

We prescribe $K(t)$ and $b_s(t)$ to be broadly representative of the diurnal cycle on clear days and simple enough to facilitate evaluation of (3.24). The diffusivity is assigned a constant daytime value K_d from sunrise ($t=0$) until sunset ($t=t_{\rm set}$) and a constant nighttime value K_n ($<K_d$) from sunset until the next sunrise:

$$K(t) = \begin{cases} K_d, & 0 \le t < t_{\rm set}, \\ K_n, & t_{\rm set} \le t < t_{24}. \end{cases} \tag{4.1}$$

The decrease in turbulent diffusivity from day to night is quantified through

$$\varepsilon \equiv \frac{K_n}{K_d}. \tag{4.2}$$

The surface buoyancy is specified as the piecewise linear (sawtooth) function

$$b_s(t) = \begin{cases} b_{\rm min} + \Delta b\left(\dfrac{t}{t_{\rm max}}\right), & 0 \le t < t_{\rm max}, \\ b_{\rm max} - \Delta b\left(\dfrac{t-t_{\rm max}}{t_{24}-t_{\rm max}}\right), & t_{\rm max} \le t < t_{24}, \end{cases} \tag{4.3}$$

where $\Delta b \equiv b_{\rm max} - b_{\rm min}$, $b_{\rm min}$ is the buoyancy minimum, which occurs at sunrise, and $b_{\rm max}$ is the buoyancy maximum, which occurs a few hours before sunset, at time $t_{\rm max}$. Sawtooth functions provide reasonable representations of the diurnal temperature/buoyancy cycle on clear days (Sanders 1975; Reicosky et al. 1989; Sadler and Schroll 1997). Schematics of $K(t)$ and $b_s(t)$ are given in Fig. 2.

With the above specifications, $\kappa(t)$ in (3.19) is evaluated as

$$\kappa(t) = \begin{cases} \dfrac{K_d}{\overline{K}}t, & 0 \le t < t_{\rm set}, \\ \dfrac{K_d t_{\rm set} + K_n(t-t_{\rm set})}{\overline{K}}, & t_{\rm set} \le t < t_{24}, \end{cases} \tag{4.4}$$

where

$$\overline{K} \equiv K_d t_{\rm set}/t_{24} + K_n(1 - t_{\rm set}/t_{24}), \tag{4.5}$$

and $D_{j,m}$ in (3.24) is evaluated as

$$\begin{aligned} D_{j,m} = \frac{K_d}{\overline{K}\phi_j t_{24}}\Bigg\{ & \Delta b\sin\alpha\frac{(\phi_j t_{\rm max}-1)\exp(\phi_j t_{\rm max})+1}{\phi_j t_{\rm max}} + (b_{\rm min}\sin\alpha - l_j v_G)[\exp(\phi_j t_{\rm max})-1] \\ & + \Delta b\sin\alpha\frac{(\phi_j t_{\rm max}-1)\exp(\phi_j t_{\rm max}) - (\phi_j t_{\rm set}-1)\exp(\phi_j t_{\rm set})}{\phi_j(t_{24}-t_{\rm max})} \\ & + \left(b_{\rm max}\sin\alpha - l_j v_G + \frac{t_{\rm max}\Delta b\sin\alpha}{t_{24}-t_{\rm max}}\right)[\exp(\phi_j t_{\rm set}) - \exp(\phi_j t_{\rm max})]\Bigg\} \\ & + \frac{K_n}{\overline{K}\eta_j t_{24}}\exp[(\mu_j - 2m\pi i/t_{24})t_{\rm set}(1-\varepsilon)K_d/\overline{K}]\Bigg\{\Delta b\sin\alpha\frac{(\eta_j t_{\rm set}-1)\exp(\eta_j t_{\rm set}) - (\eta_j t_{24}-1)\exp(\eta_j t_{24})}{\eta_j(t_{24}-t_{\rm max})} \\ & + \left(b_{\rm max}\sin\alpha - l_j v_G + \frac{t_{\rm max}\Delta b\sin\alpha}{t_{24}-t_{\rm max}}\right)[\exp(\eta_j t_{24}) - \exp(\eta_j t_{\rm set})]\Bigg\}, \end{aligned} \tag{4.6}$$

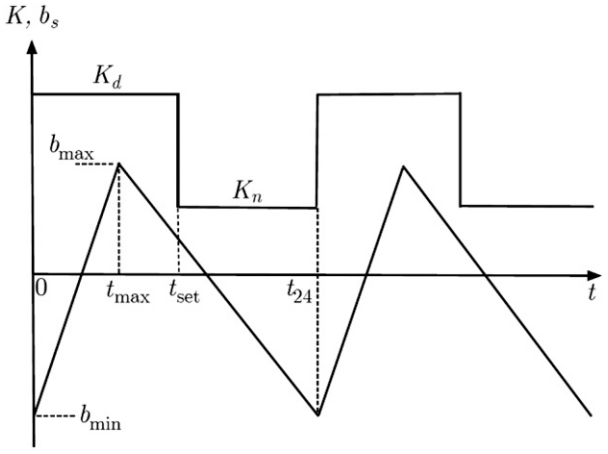

FIG. 2. Schematic of the diurnally varying diffusivity $K(t)$ and surface buoyancy $b_s(t)$ functions considered in section 4. The diffusivity varies as a step function with daytime value K_d and nighttime value K_n. The surface buoyancy varies as a sawtooth function that increases from a minimum $b_{\min}$ at sunrise ($t = 0$) to a maximum $b_{\max}$ at time $t_{\max}$, a few hours before sunset (time t_{set}).

where

$$\phi_j \equiv -\mu_j + (\mu_j - 2m\pi i/t_{24})K_d/\overline{K} \quad \text{and} \tag{4.7}$$

$$\eta_j \equiv -\mu_j + \varepsilon(\mu_j - 2m\pi i/t_{24})K_d/\overline{K}. \tag{4.8}$$

Use of these analytical expressions obviates the need for numerical integration in the evaluation of (3.17). The resulting solution is independent of the spatial and temporal resolution of the grid on which it is evaluated, but grid resolution should be considered when graphing or taking finite differences of the solution.

Although we have not proved that the F_m form a complete set, we can show that the lower conditions (2.5) and (2.6) can be recovered to any desired accuracy by including a sufficiently large number of terms in the finite series approximation of (3.17) with $D_{j,m}$ given by (4.6). An example is shown in Fig. 3.

b. Reference experiment BH

In each experiment, the analytical solution was evaluated for one 24-h period at 10-min intervals with a grid spacing of $\Delta z = 20$ m. The series in (3.17) were truncated at $|m| \le 20\,000$. A reference experiment BH (B for Blackadar mechanism and H for Holton mechanism) was designed to provide a baseline description of fair weather warm-season diurnal cycles over the sloping portion of the southern Great Plains (e.g., in western Oklahoma), where both Blackadar and Holton mechanisms are present. The parameters in BH are also the default parameters in all of the other experiments.

In BH we take $f = 8.6 \times 10^{-5}\,\text{s}^{-1}$ and $\alpha = 0.15°$, values that are appropriate for western Oklahoma (36.4°N, 99.4°W). The 0.15° slope is also close to the 1/400 slope used in H67. We take $t_{\text{set}} = 12$ h based on the approximate times of sunrise [0630 central standard time (CST)] and sunset (1830 CST) in late September at the chosen location (U.S. Naval Observatory 2016). From an observed $9.3\,\text{m s}^{-1}$ diurnal range of surface geostrophic winds (described in appendix A), we calculate a diurnal range of surface buoyancy of $0.4\,\text{m s}^{-2}$. We split this range equally between a peak of $b_{\max} = 0.2\,\text{m s}^{-2}$ at

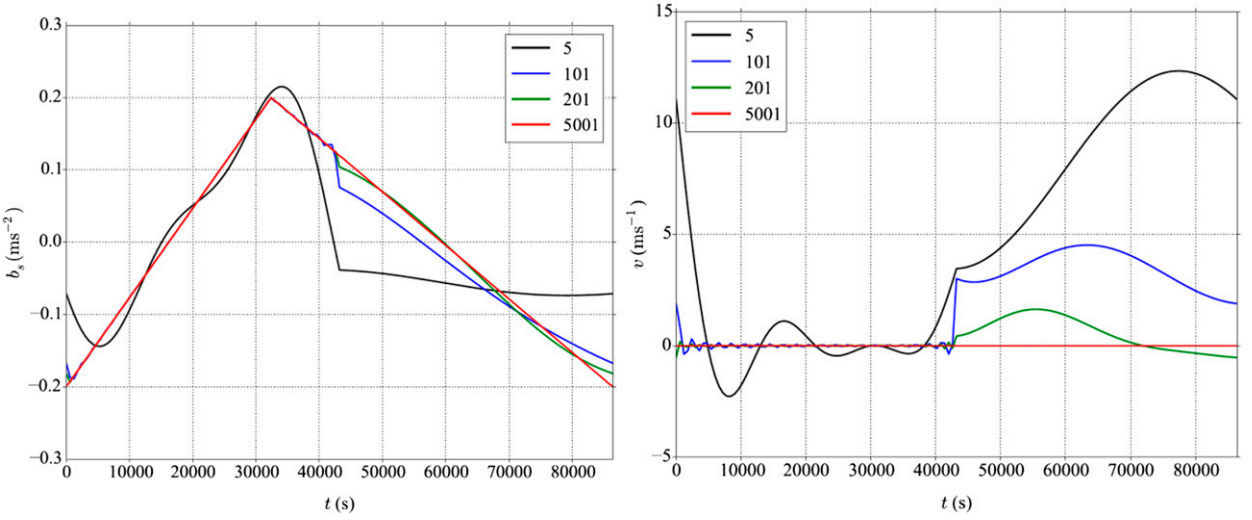

FIG. 3. Time dependence of (left) b and (right) v on the slope ($z = 0$) computed using a progressively larger number of terms (see legends) in the truncated series form of (3.17) for experiment BH. As more terms are included, the variables approach their appropriate slope distributions: no slip for v, and sawtooth function for b, with $b_{\min} = -0.2\,\text{m s}^{-2}$ and $b_{\max} = 0.2\,\text{m s}^{-2}$.

TABLE 1. Parameters in reference experiment BH. Times are in hours after sunrise. Sunrise is at ~0630 CST.

Parameter	Value
f	$8.6 \times 10^{-5}\,\mathrm{s}^{-1}$ (at $\varphi = 36.4°\mathrm{N}$)
v_G	$10\,\mathrm{m\,s}^{-1}$
α	0.15°
N	$0.01\,\mathrm{s}^{-1}$
$b_{\max}$	$0.2\,\mathrm{m\,s}^{-2}$
$b_{\min}$	$-0.2\,\mathrm{m\,s}^{-2}$
$t_{\max}$	9 h
t_{set}	12 h
K_d	$100\,\mathrm{m}^2\,\mathrm{s}^{-1}$
K_n	$1\,\mathrm{m}^2\,\mathrm{s}^{-1}$
δ	$0.2\,\mathrm{day}^{-1}$

$t_{\max} = 9$ h (3 h before sunset) and a sunrise minimum of $b_{\min} = -0.2\,\mathrm{m\,s}^{-2}$ but will consider unequal magnitudes of $b_{\max}$ and $b_{\min}$ in the sensitivity experiments. At sunset the diffusivity drops from $K_d = 100\,\mathrm{m}^2\,\mathrm{s}^{-1}$ to $K_n = 1\,\mathrm{m}^2\,\mathrm{s}^{-1}$, values that are within the range of published estimates of K for the daytime convective atmospheric boundary layer and the nocturnal stable boundary layer, respectively, cited in Shapiro and Fedorovich (2010). We adopt typical free-atmosphere values for N ($=0.01\,\mathrm{s}^{-1}$) and v_G ($=10\,\mathrm{m\,s}^{-1}$). The radiative damping parameter $\delta = 0.2\,\mathrm{day}^{-1}$ is the same as in Egger (1985). These parameters are summarized in Table 1.

Figures 4–8 show that BH provides a qualitatively reasonable depiction of the diurnal cycle of the wind and buoyancy in the atmospheric boundary layer, including the development and breakup of both a nocturnal stable boundary layer and a low-level jet. The low-level wind speeds shown in Fig. 4 are subgeostrophic and relatively steady during most of the afternoon (15 000 s until sunset) but thereafter increase rapidly in strength and become supergeostrophic. After sunset, the height of the wind maximum descends until ~65 000 s and thereafter remains at ~480 m for several hours. The peak speed of $\sim 21\,\mathrm{m\,s}^{-1}$ puts the modeled jet (barely) into the strongest category (category 3) of the Bonner (1968), Whiteman et al. (1997), and Song et al. (2005) classification systems. The peak speed occurs at $t = \sim 73\,800$ s, 3 h after midnight (CST). Figure 5 shows the evolution of $v(z)$ from a broad relatively weak late-afternoon profile to the graceful jetlike shape characteristic of LLJs. At the time of the speed maximum (roughly the time of curve d in Fig. 5), the peak speed is almost entirely associated with the v wind component[5] (this is also evident from the 500-m hodograph curve in Fig. 6). Figure 5 also shows the postsunset development of upslope winds, with a peak magnitude of $\sim 10\,\mathrm{m\,s}^{-1}$ reached approximately 3 h after sunset. The hodographs in Fig. 6 show an anticyclonic turning of the wind vectors from sunset until sunrise. During this period the hodographs are approximately semicircles reminiscent of IOs, although the curves become increasingly asymmetrical at lower levels. The shortness of the hodograph segments between the times of peak surface buoyancy and sunset further indicate that the late-afternoon winds are in a near-steady state. Figures 7 and 8 show the development of a shallow nocturnal stable boundary layer, with negative buoyancies extending up to ~200 m at the time of the speed maximum. Shortly after sunrise, mixing spreads the negatively buoyant air upward and dilutes the cold layer. By late morning, the boundary layer is dominated by positive buoyancy.

c. *Pure Blackadar- and Holton-mechanism experiments*

Experiments were conducted to gauge the separate effects of the Blackadar and Holton mechanisms. The Blackadar mechanism was simulated by turning off the Holton mechanism (setting $\alpha = 0°$, which decouples the wind and buoyancy fields), and the Holton mechanism was simulated by turning off the Blackadar mechanism (setting $K_d = K_n = K$).[6] We focus on the peak v wind component $v_{\max}$ (which, as noted, differed from the wind speed by less than $1\,\mathrm{m\,s}^{-1}$), and the height $Z_{v_{\max}}$ and time $T_{v_{\max}}$ at which this peak v is attained. The results are summarized in Table 2. In Blackadar-mechanism experiment B, $v_{\max}$ is $4.3\,\mathrm{m\,s}^{-1}$ weaker than in BH. In a second Blackadar-mechanism experiment ($\mathrm{B}v_G^+$), a 50% increase in v_G yields a corresponding ~50% increase in $v_{\max}$ over that in B, with essentially no change in $Z_{v_{\max}}$ or $T_{v_{\max}}$. Holton-mechanism experiments were conducted using $K = 1\,\mathrm{m}^2\,\mathrm{s}^{-1}$ (weak-mixing experiment $\mathrm{H}K^-$), $K = 10\,\mathrm{m}^2\,\mathrm{s}^{-1}$ (moderate-mixing experiment H), and $K = 100\,\mathrm{m}^2\,\mathrm{s}^{-1}$ (strong-mixing experiment $\mathrm{H}K^+$). The corresponding $v_{\max}$ values were remarkably similar to each other ($\sim 11\,\mathrm{m\,s}^{-1}$) and were significantly less than $v_{\max}$ in B and BH. However, despite the similarity of the $v_{\max}$ values, $Z_{v_{\max}}$ varied by an order of magnitude, from 320 m in $\mathrm{H}K^-$ to 3160 m in $\mathrm{H}K^+$. In a final Holton-mechanism experiment ($\mathrm{H}b_{\max}^+$) with

[5] In BH and all of the upcoming experiments, the difference between the peak v wind component and the wind speed $\sqrt{u^2 + v^2}$ at the time of peak v was typically $\sim 0.5\,\mathrm{m\,s}^{-1}$ and always less than $1\,\mathrm{m\,s}^{-1}$.

[6] More accurately, to avoid the 0/0 computational difficulty that arises in the evaluation of (4.6) when K_d is set exactly equal to K_n, we take K_d to differ from K_n by a physically insignificant amount, $0.0001\,\mathrm{m}^2\,\mathrm{s}^{-1}$.

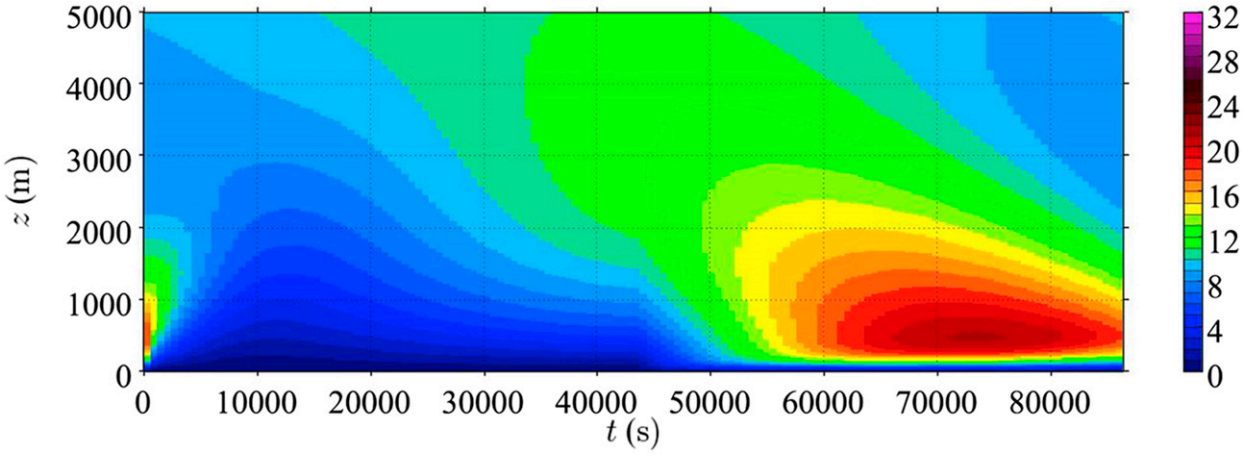

FIG. 4. Wind speed ($m\,s^{-1}$) as a function of height and time over a 24-h period in experiment BH. Sunrise is at $t = 0$ s. Sunset is at $t_{set} = 43\,200$ s. The surface buoyancy peaks at $t_{max} = 32\,400$ s.

moderate mixing ($K = 10\,m^2\,s^{-1}$, as in H) and larger surface buoyancy ($b_{max} = 0.3\,m\,s^{-2}$, 50% larger than in H), v_{max} only increased by $1.3\,m\,s^{-1}$ (~10%) over v_{max} in H. In short, the Holton mechanism produced wind maxima that were notably weaker than those produced by the Blackadar mechanism. We also note that the $T_{v_{max}}$ in the Blackadar-mechanism experiments exceeded those in the Holton-mechanism experiments by more than 3 h and exceeded $T_{v_{max}}$ in BH by 0.5 h. The relative strengths and timings of the wind maxima in these experiments are in qualitative agreement with the results of Du and Rotunno (2014, Fig. 5).

d. *Exploring the parameter space*

We now examine the sensitivity of the solution to the governing parameters. Table 3 summarizes experiments in which one parameter is varied and the others are fixed at their reference values. The experiment names are of the form BH$\gamma^{\pm}$, where γ represents the varied parameter, and the plus-or-minus symbol indicates that the magnitude of that parameter is larger (+) or smaller (−) than in BH.

The evolution of the jet heights in these experiments was remarkably similar to that in BH: the wind maxima descended rapidly after sunset, leveled off to a near-constant height by the time of peak jet intensity, and

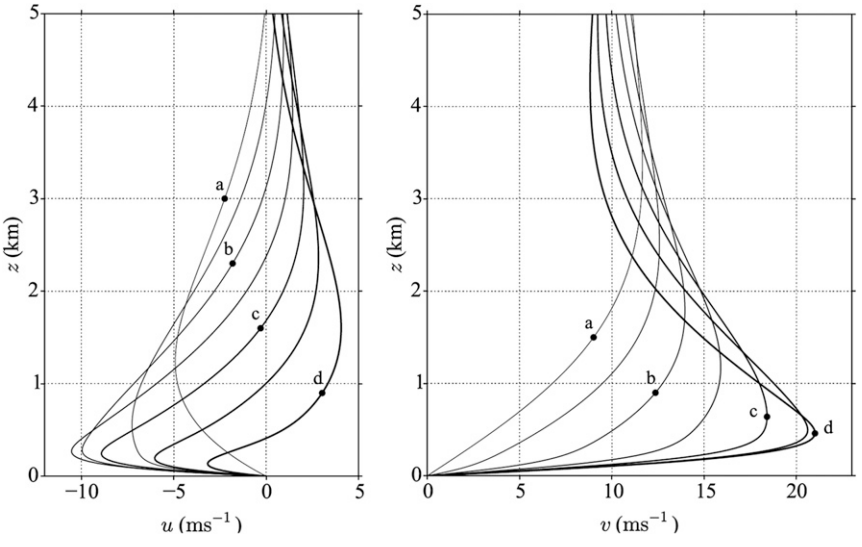

FIG. 5. Postsunset evolution of (left) $u(z)$ and (right) $v(z)$ profiles in experiment BH. Curves are shown at 1.5-h intervals starting from sunset. Labeled curves correspond to times t_{set} (line a), $t_{set} + 3$ h (line b), $t_{set} + 6$ h (line c), and $t_{set} + 9$ h (line d).

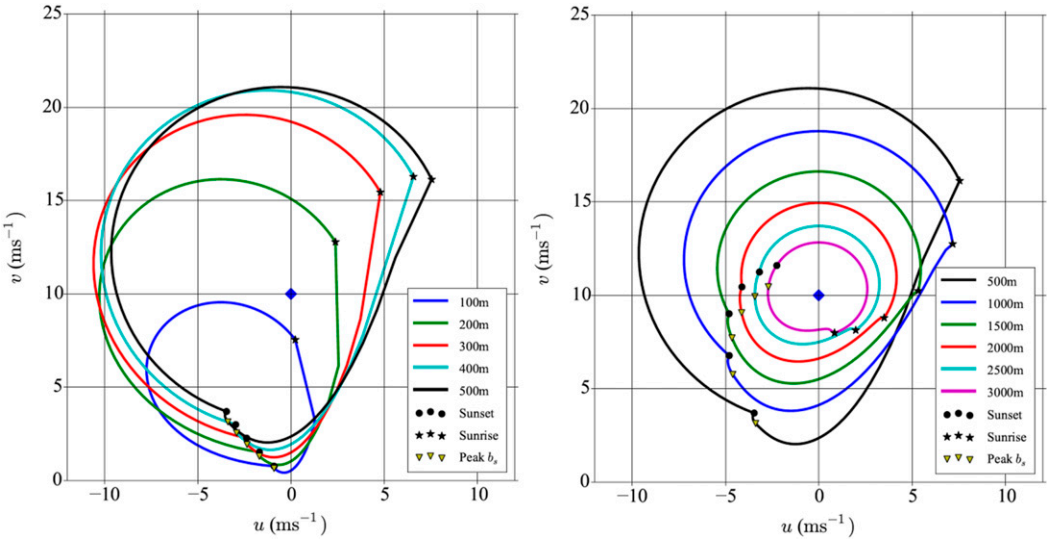

FIG. 6. Evolution of the wind hodographs in experiment BH over a 24-h period at different heights. Curves are plotted (left) at low levels in 100-m increments up to the jet maximum and (right) at and above the jet maximum in 500-m increments. The times of sunset, sunrise, and peak surface buoyancy are indicated on the hodographs. The blue diamond indicates the geostrophic wind.

stayed close to that height for the rest of the night. In most experiments, $Z_{v_{\max}}$ was in a narrow range between 440 and 520 m. A notable exception was in the nighttime diffusivity experiments, where a large diffusivity $K_n = 5\,\mathrm{m^2\,s^{-1}}$ (in BHK_n^+) yielded a large $Z_{v_{\max}}$ (900 m), and a small diffusivity $K_n = 0.2\,\mathrm{m^2\,s^{-1}}$ (in BHK_n^-) yielded a small $Z_{v_{\max}}$ (240 m). In light of these results, the tendencies noted in Steeneveld et al. (2008), Storm et al. (2009), and Werth et al. (2011) for their regional model-simulated jets to be too deep suggests that the parameterized mixing in those simulations may have been too aggressive at night.

The time $T_{v_{\max}}$ was relatively insensitive to most of the parameters, generally being well within an hour of $T_{v_{\max}}$ in BH. An exception was, not surprisingly, in experiments BHt_{set}^+ and BHt_{set}^-, where shifting T_{set} later or earlier by 2 h shifted $T_{v_{\max}}$ later or earlier by ~2 h. Also, in BHf^+ and BHf^-, $T_{v_{\max}}$ decreased with increasing latitude, in qualitative accord with the IO and inertia–gravity oscillation theories. More specifically, the ratio of the inertial period $2\pi/f$ in BHf^+ to that in BHf^- (~0.753) was close to the ratio of the time intervals $T_{v_{\max}} - T_{\mathrm{set}}$ in those experiments (~0.786). An even better agreement with the latter ratio was obtained using the ratio of the inertia–gravity oscillation period $2\pi/\sqrt{f^2 + N^2\sin^2\alpha}$ (Shapiro and Fedorovich 2009) in BHf^+ to that in BHf^- (~0.772).

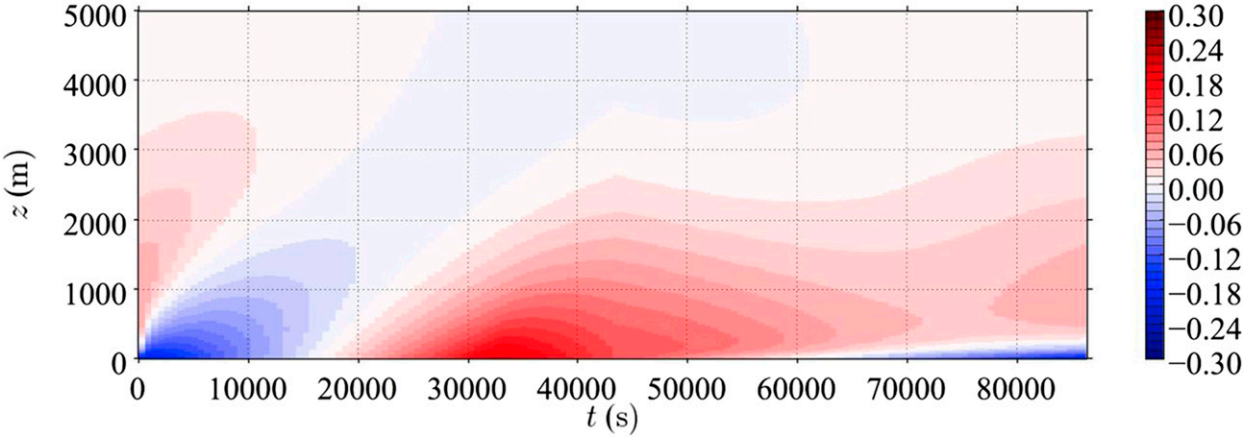

FIG. 7. As in Fig. 4, but for b ($\mathrm{m\,s^{-2}}$).

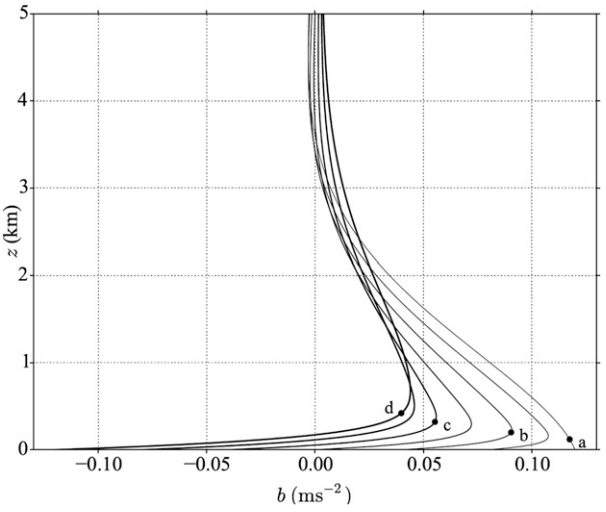

FIG. 8. As in Fig. 5, but for $b(z)$ profiles.

There are many interesting aspects to the jet strength sensitivities:

(i) The value of v_{max} was very sensitive to v_G (cf. BHv_G^- and BHv_G^+). A strong dependence of jet strength on geostrophic wind is a hallmark of the IO theory (implied in Fig. 10 of B57 and explicit in the analytical solution of Shapiro and Fedorovich 2010). The importance of a strong mean background wind (or geostrophic wind) to jet strength has also been recognized by Wexler (1961), Arritt et al. (1997), Zhong et al. (1996), Jiang et al. (2007), and Parish and Oolman (2010).

(ii) Larger values of v_{max} were also associated with larger values of b_{max}. Recall that in the pure Holton-mechanism experiments, increasing b_{max} to $0.3\,m\,s^{-2}$ only produced a $1.3\,m\,s^{-1}$ increase in v_{max} (Hb_{max}^+ vs H). Since the same increase in b_{max} now increases v_{max} by $3.6\,m\,s^{-1}$ (BHb_{max}^+ vs BH), we see that the interaction of the Holton mechanism with the Blackadar mechanism is cooperative, at least with respect to the role of daytime heating.

(iii) Although the solution is less sensitive to b_{min} than it is to b_{max}, increasing the magnitude of b_{min} (greater nighttime cooling) actually decreases v_{max} (BHb_{min}^- vs BHb_{min}^+). This is consistent with Parish and Oolman's (2010) finding that nocturnal cooling is inimical to the LLJ. It should be borne in mind, however, that in real atmospheric boundary layers, nocturnal cooling also affects the level of turbulence, and it is somewhat artificial to vary the diffusivities independently of the buoyancy parameters.

(iv) Consistent with the B57–BB57 theory, the jet winds intensify with an increasing day-to-night ratio of diffusivities (decreasing ε), associated with either an increase in the daytime diffusivity (in BHK_d^+) or decrease in the nighttime diffusivity (in BHK_n^-).

(v) As in H67 and Shapiro and Fedorovich (2009), the jet strengthens as the stratification weakens (BHN^+ vs BHN^-). In further experiments (Fig. 9), unphysically large values of v_{max} are obtained in the (unrealistic) case of a neutrally stratified free atmosphere ($N = 0\,s^{-1}$).

(vi) There is a slight increase in v_{max} as the lag between the time of peak surface buoyancy and sunset is decreased, either through increasing t_{max} (in BHt_{max}^+) or decreasing t_{set} (in BHt_{set}^-).

(vii) Although provision for radiative damping was essential to obtain purely periodic solutions (section 3), these periodic solutions exhibit little sensitivity to the actual value of the damping parameter; varying δ by an order of magnitude changed v_{max} by less than $1\,m\,s^{-1}$ (cf. BH$_\delta^+$ and BH$_\delta^-$). A lack of sensitivity to δ was also reported in Egger's (1985) katabatic flow study.

(viii) Further experiments (Fig. 9) reveal a strong dependence of v_{max} on slope angle. For a realistic free-atmosphere stratification ($N = 0.01\,s^{-1}$), v_{max} increases from $16.8\,m\,s^{-1}$ (its value in B) at $\alpha = 0°$ to a local maximum of $\sim 21.6\,m\,s^{-1}$ for α

TABLE 2. Characteristics of the modeled LLJ in a set of Blackadar-mechanism ($\alpha = 0°$) and Holton-mechanism ($K_d = K_n = K$) experiments. Parameters are as in experiment BH (Table 1), except where noted. The peak v (v_{max}) is found at height $Z_{v_{max}}$ at time $T_{v_{max}}$. Times are in hours after sunrise. Sunrise is at ~0630 CST.

Expt	Description	v_{max} ($m\,s^{-1}$)	$Z_{v_{max}}$ (m)	$T_{v_{max}}$ (h)
BH	Reference experiment	21.1	480	20.5
B	Blackadar	16.8	460	21.0
Bv_G^+	Blackadar with strong geostrophic wind ($v_G = 15\,m\,s^{-1}$)	25.2	460	21.0
H	Holton with moderate mixing ($K = 10\,m^2\,s^{-1}$)	11.5	1000	17.8
HK^+	Holton with strong mixing ($K = 100\,m^2\,s^{-1}$)	11.3	3160	17.8
HK^-	Holton with weak mixing, ($K = 1\,m^2\,s^{-1}$)	11.5	320	17.8
Hb_{max}^+	Holton with moderate mixing ($K = 10\,m^2\,s^{-1}$) and strong surface heating ($b_{max} = 0.3\,m\,s^{-2}$)	12.8	940	17.7

TABLE 3. Sensitivity of modeled LLJ characteristics to the governing parameters. In each experiment, one parameter is varied from its value in experiment BH (Table 1). Times are in hours after sunrise. Sunrise is at ~0630 CST.

Varied parameter	Expt	Parameter value	v_{max} (m s^{-1})	$Z_{v_{max}}$ (m)	$T_{v_{max}}$ (h)
None	BH	—	21.1	480	20.5
b_{max}	BHb^+_{max}	0.3 m s^{-2}(Δb = 0.5 m s^{-2})	24.7	480	20.5
	BHb^-_{max}	0.0 m s^{-2}(Δb = 0.2 m s^{-2})	14.0	480	20.7
b_{min}	BHb^+_{min}	−0.3 m s^{-2}(Δb = 0.5 m s^{-2})	20.4	480	20.5
	BHb^-_{min}	0.0 m s^{-2}(Δb = 0.2 m s^{-2})	22.6	460	20.7
K_d	BHK^+_d	500 m^2 s^{-1} (ε = 0.002)	22.8	540	21.2
	BHK^-_d	20 m^2 s^{-1} (ε = 0.05)	18.3	400	19.7
K_n	BHK^+_n	5 m^2 s^{-1} (ε = 0.05)	18.2	900	19.7
	BHK^-_n	0.2 m^2 s^{-1} (ε = 0.002)	22.8	240	21.2
v_G	BHv^+_G	15 m s^{-1}	28.8	460	20.7
	BHv^-_G	5 m s^{-1}	13.4	480	20.5
f	BHf^+	9.7 × 10^{-5} s^{-1} (φ = 42°N)	20.8	440	19.7
	BHf^-	7.3 × 10^{-5} s^{-1} (φ = 30°N)	21.7	520	21.8
δ	BHδ^+	1 day^{-1}	20.4	460	20.5
	BHδ^-	0.1 day^{-1}	21.2	480	20.5
t_{max}	BHt^+_{max}	11 h ($t_{set} - t_{max}$ = 1 h)	22.5	440	20.7
	BHt^-_{max}	7 h ($t_{set} - t_{max}$ = 5 h)	19.7	480	20.5
t_{set}	BHt^+_{set}	14 h ($t_{set} - t_{max}$ = 5 h)	19.1	500	22.5
	BHt^-_{set}	10 h ($t_{set} - t_{max}$ = 1 h)	22.6	440	18.7
N	BHN^+	0.02 s^{-1}	17.0	460	19.7
	BHN^-	0.005 s^{-1}	22.5	480	20.8

between 0.2° and 0.3°. Similar optimal values of α were obtained in Shapiro and Fedorovich (2009). The optimal value is in qualitative agreement with climatological studies (Bonner 1968; Walters et al. 2008), though with the preferred longitudes of LLJ occurrence in those studies associated with slope angles somewhat lower (terrain farther east) than indicated here. It should be kept in mind, however, that while we fixed v_G at its value in BH, the summer-mean geostrophic wind—which affects jet strength—undergoes significant spatial variation across the Great Plains (Jiang et al. 2007; Pu and Dickinson 2014; Du and Rotunno 2014).

In a final experiment, we increased the values of two parameters that individually had a large impact on jet strength. Setting $v_G = 15\,\mathrm{m\,s^{-1}}$ and $b_{max} = 0.3\,\mathrm{m\,s^{-2}}$ produced an intense jet, with $v_{max} \approx 32\,\mathrm{m\,s^{-1}}$ (Fig. 10). LLJ winds of this magnitude, though infrequent, do occur over the southern Great Plains (Bonner et al. 1968, their Fig. 2; Whiteman et al. 1997, their Fig. 11; Song et al. 2005, their Fig. 2).

5. Summary and future work

Our theory for the Great Plains nocturnal LLJ combines the Blackadar mechanism for IOs arising from a sudden decrease of turbulent mixing at sunset, with the Holton mechanism for an oscillation arising from the diurnal heating/cooling of a sloping surface. Periodic solutions of the 1D Boussinesq equations of motion and thermal energy for a stably stratified fluid were obtained analytically for the combined mechanisms, with the separate mechanisms studied as particular cases.

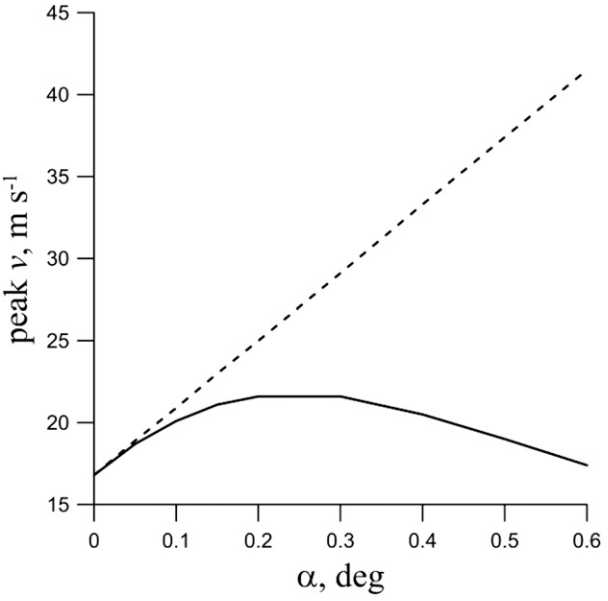

FIG. 9. Peak v as a function of slope angle for $N = 0.01\,\mathrm{s^{-1}}$ (solid curve) and $N = 0.0\,\mathrm{s^{-1}}$ (dashed curve). Other parameters are as in experiment BH.

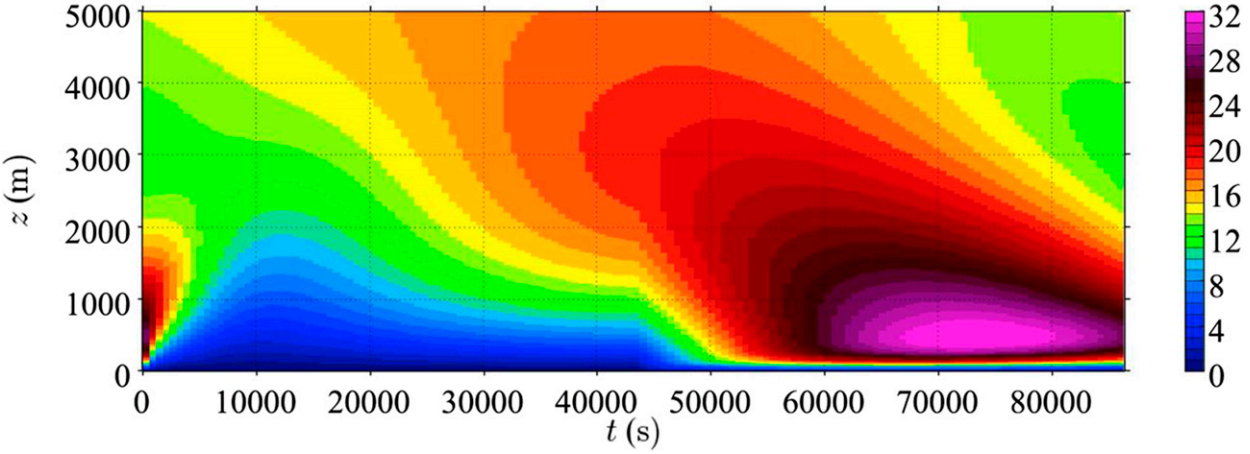

FIG. 10. Wind speed ($m\,s^{-1}$) as a function of height and time over a 24-h period for an intense jet associated with strong surface buoyancy ($b_{max} = 0.3\,m\,s^{-2}$) and a strong geostrophic wind ($v_G = 15\,m\,s^{-1}$). Other parameters are as in experiment BH. Sunrise is at $t = 0$ s. Sunset is at $t_{set} = 43\,200$ s. The surface buoyancy peaks at $t_{max} = 32\,400$ s.

In the context of our 1D model, provision for a radiative damping term (Newtonian heating/cooling) in the thermal energy equation was essential for periodic solutions to exist. The model jets exhibited little sensitivity to the actual value of the damping parameter.

A reference experiment in which both mechanisms were operating provided a baseline description of the fair-weather warm-season diurnal cycle over the sloping portion of the southern Great Plains, including the emergence of a strong LLJ in the nocturnal phase of the diurnal cycle. The strength, timing, and vertical structure of the analytical LLJ were in good qualitative agreement with typical LLJ observations over the southern Great Plains.

Experiments were conducted with the Holton and Blackadar mechanisms operating separately. The Holton mechanism tended to produce relatively weak jets. The Blackadar mechanism produced jets that were roughly 50% stronger than in the Holton-mechanism experiments. In a combined Holton- and Blackadar-mechanism experiment (the reference experiment), the peak winds increased by ~25% over those in the Blackadar-mechanism experiment. These strongly supergeostrophic winds (marginally) exceeded the theoretical 100% supergeostrophic limit for the Blackadar mechanism.

Sensitivity tests with the 11 governing parameters showed that the height of the wind maxima evolved in remarkably similar fashion for all parameter combinations: a rapid descent after sunset, followed by a leveling off to a near-constant value through much of the night. This equilibrium height was relatively insensitive to all parameters except the nighttime diffusivity, larger values of which were associated with higher jets. Jet wind speeds increased with increasing geostrophic wind, increasing maximum surface buoyancy, and increasing day-to-night ratio of the diffusivities. The peak winds were maximized for small slope angles characteristic of the Great Plains, although with a small westward bias relative to climatologies. Peak speeds decreased with increasing free-atmosphere stratification and increasing magnitude of minimum slope buoyancy (strength of nocturnal cooling).

We plan to test the unified LLJ model predictions against observations from the Plains Elevated Convection at Night (PECAN) field project, run from 1 June–15 July 2015. The PECAN campaign included the deployment of fixed and mobile Doppler radars, Doppler lidars, radiosonde systems, experimental profiling sensors, and research aircraft over a domain extending from northern Oklahoma through south-central Nebraska. Wind and thermodynamic profiles through many LLJs were obtained during the course of the project.

Finally, we note several possible extensions of our 1D theory. First, as discussed in section 2a, a time-dependent free-atmosphere geostrophic wind can, in principle, be incorporated into a revised 1D analysis. In addition, it may be possible to make provision for a free-atmosphere geostrophic wind that varies linearly with height. This would extend the theory to cases where background (nonterrain associated) synoptic-scale baroclinicity is important. It also appears likely that the theory can be revised to take surface roughness into account. To accomplish this, the surface boundary conditions would need to be reformulated as normal

gradient conditions using bulk parameterizations for the momentum and heat fluxes (Stull 1988), although to keep the analysis tractable these conditions would have to be linearized. The surface drag coefficient and surface heat exchange coefficient would then appear as input parameters.

Acknowledgments. We thank the anonymous referees and Joshua Gebauer for their constructive comments and suggestions for extending the theory. This research was supported by the National Science Foundation under Grant AGS-1359698.

APPENDIX A

Geostrophic Wind, Thermal Wind, and Buoyancy in a Sloping Atmospheric Boundary Layer

In our 1D theory of the sloping atmospheric boundary layer, all variables are independent of the cross-slope coordinate, and the geostrophic wind V_G blows parallel to the terrain isoheights. We assume that V_G approaches a constant value v_G far above the slope but do not otherwise specify its spatial (height) or temporal dependencies. As we now show, the evolving V_G profile can be simply related to the buoyancy field.

By definition, V_G is related to the true horizontal (x^*) component of the perturbation pressure gradient by

$$V_G = \frac{1}{f}\frac{\partial \Pi}{\partial x^*}, \tag{A.1}$$

where we have approximated the true Coriolis parameter by $f \equiv 2\boldsymbol{\Omega}\cdot\mathbf{k}$ (see section 2a). With the help of Fig. 1, we find that

$$\begin{aligned}\frac{\partial \Pi}{\partial x^*} &= \mathbf{i}^*\cdot\nabla\Pi = \mathbf{i}^*\cdot\left(\mathbf{i}\frac{\partial \Pi}{\partial x}+\mathbf{k}\frac{\partial \Pi}{\partial z}\right)\\ &= \cos\alpha\frac{\partial \Pi}{\partial x}+\sin\alpha\frac{\partial \Pi}{\partial z}.\end{aligned} \tag{A.2}$$

Application of (2.3) in (A.2) yields

$$\frac{\partial \Pi}{\partial x^*} = \cos\alpha\left(\frac{\partial \Pi}{\partial x}+b\sin\alpha\right) \simeq \frac{\partial \Pi}{\partial x}+b\sin\alpha, \tag{A.3}$$

where $\cos\alpha \simeq 1$ is a suitable approximation for the Great Plains. Since b is independent of x, and $\partial\Pi/\partial x$ is independent of x and z (see section 2a), (A.3) shows that $\partial\Pi/\partial x^*$—and thus V_G—are, at most, functions of z and t. Furthermore, since $\partial\Pi/\partial x$ is independent of x and z, and $b \to 0$ far above the slope,

$$\frac{\partial \Pi}{\partial x}(\text{at any } z) = \lim_{z\to\infty}\frac{\partial \Pi}{\partial x} \simeq \lim_{z\to\infty}\frac{\partial \Pi}{\partial x^*} = \lim_{z\to\infty} fV_G = fv_G. \tag{A.4}$$

Applying (A.4) in (A.3) and substituting the resulting expression into (A.1) then yields

$$V_G(z,t) = v_G + \frac{\sin\alpha}{f}b(z,t). \tag{A.5}$$

To guide the specification of the surface buoyancy parameters in our experiments, we used (A.5) together with data from Sangster's (1967) analysis of the surface geostrophic wind (which was primarily southerly) for June 1966 over a line from Oklahoma City (φ = 35.5°N) to Amarillo, Texas. Using Sangster's estimates of 18 knots (1 kt = 0.51 m s^{-1})[A1] for the mean diurnal range of the southerly surface geostrophic wind and 1/530 for the average slope of that region, (A.5) yields a diurnal range of 0.4 m s^{-2} for the surface buoyancy changes.

To get an equation for the thermal wind $\partial V_G/\partial z^*$, take the z^* derivative of (A.5) and use $\partial b/\partial z^* = \csc\alpha\,\partial b/\partial x^*$. This latter relation follows from the elimination of $\partial b/\partial z$ between the equations for the x^* and z^* derivatives of $b[z(x^*, z^*), t]$: $\partial b/\partial z^* = \partial b/\partial z\partial z/\partial z^* = \cos\alpha\,\partial b/\partial z \cong \partial b/\partial z$, and $\partial b/\partial x^* = \partial b/\partial z\partial z/\partial x^* = \sin\alpha\,\partial b/\partial z$. We obtain

$$\frac{\partial V_G}{\partial z^*} = \frac{1}{f}\frac{\partial b}{\partial x^*}. \tag{A.6}$$

In view of (A.5) and (A.6), one may consider the thermal structure of this sloping boundary layer in terms of the buoyancy, geostrophic wind, or thermal wind.

APPENDIX B

Solution of (2.13)

We solve (2.13) using standard formulas for cubic equations (e.g., Abramowitz and Stegun 1964, pg. 17). Write (2.13) as

$$k^3 + a_2k^2 + a_1k + a_0 = 0, \tag{B.1}$$

$$a_2 \equiv 2\delta, \quad a_1 \equiv \omega^2+\delta^2, \quad a_0 \equiv \delta N^2\sin^2\alpha, \tag{B.2}$$

[A1] Bonner and Paegle (1970) estimated a similar diurnal range (8 m s^{-1}) for the southerly surface geostrophic wind in the same area considered by Sangster (1967), but for a 1-week period in August 1960.

and define

$$q \equiv \frac{1}{3}a_1 - \frac{1}{9}a_2^2 = \frac{1}{3}\omega^2 - \frac{1}{9}\delta^2, \tag{B.3}$$

$$r \equiv \frac{1}{6}(a_1 a_2 - 3a_0) - \frac{1}{27}a_2^3 = \delta\left(\frac{1}{3}\omega^2 - \frac{1}{2}N^2\sin^2\alpha + \frac{1}{27}\delta^2\right), \tag{B.4}$$

$$\Delta \equiv q^3 + r^2 = \frac{\omega^2}{27}(\omega^2+\delta^2)^2 - \delta^2 N^2 \sin^2\alpha\left(\frac{1}{3}\omega^2 + \frac{1}{27}\delta^2 - \frac{1}{4}N^2\sin^2\alpha\right), \tag{B.5}$$

and

$$s_1 \equiv (r + \Delta^{1/2})^{1/3}, \quad s_2 \equiv (r - \Delta^{1/2})^{1/3}. \tag{B.6}$$

The roots of (2.13) can then be written as

$$k_1 = (s_1 + s_2) - \frac{a_2}{3}, \tag{B.7}$$

$$k_2 = -\frac{1}{2}(s_1 + s_2) - \frac{a_2}{3} + \frac{i\sqrt{3}}{2}(s_1 - s_2), \quad \text{and} \tag{B.8}$$

$$k_3 = -\frac{1}{2}(s_1 + s_2) - \frac{a_2}{3} - \frac{i\sqrt{3}}{2}(s_1 - s_2). \tag{B.9}$$

For a typical free-atmosphere value of N ($\sim 0.01\,\mathrm{s}^{-1}$), Great Plains slope $\alpha \sim 0.2°$, and latitudes spanning the Great Plains across North America ($30° < \varphi < 60°$N), $\omega^2 = N^2\sin^2\alpha + f^2$ ranges from $O(10^{-9})$ to $O(10^{-8})\,\mathrm{s}^{-2}$ (and obviously $N^2\sin^2\alpha < \omega^2$). For damping parameters δ in a range from 0.1 to $1\,\mathrm{day}^{-1}$ that includes values estimated by Kuo (1973) and the value $0.2\,\mathrm{day}^{-1}$ adopted by Egger (1985), δ^2 ranges from $\sim 10^{-12}$ to $\sim 10^{-10}\,\mathrm{s}^{-2}$, so $\delta^2 \ll \omega^2$ by one to four orders of magnitude. In view of that inequality, we see from (B.5) that $\Delta > 0$, while a comparison of (B.5) with (B.4) shows that $\Delta^{1/2} \gg r$. Thus, $r + \Delta^{1/2}$ is positive, while $r - \Delta^{1/2}$ is negative. Taking the 1/3 power of those factors then produces a real and positive s_1 and a real and negative s_2, which we write as[B1]

$$s_1 = |r + \Delta^{1/2}|^{1/3} > 0, \quad s_2 = -|r - \Delta^{1/2}|^{1/3} < 0. \tag{B.10}$$

[B1] In the last step to (B.10), we implicitly assumed that of the three third-power roots of 1 (i.e., $\{1, e^{2\pi i/3}, e^{4\pi i/3}\}$) it suffices to choose 1, and that of the three third-power roots of -1 (i.e., $\{-1, -e^{2\pi i/3}, -e^{4\pi i/3}\}$) it suffices to choose -1. However, Jeffrey and Norman (2004) showed that, in general, not all third-power root choices for s_1 and s_2 [i.e., in (B.6)] lead to solutions of the cubic equation and that one should verify that any candidate solution really is a solution. For the examples in section 4, we verified numerically that (B.10) is correct.

Since s_1 and s_2 are real, (B.7)–(B.9) indicate that k_1 is real, while k_2 and k_3 form a complex conjugate pair.

REFERENCES

Abramowitz, M., and I. Stegun, 1964: *Handbook of Mathematical Functions with Formulas, Graphs, and Mathematical Tables*. Dover Publications, 1046 pp.

Andreas, E. L, K. J. Claffey, and A. P. Makshtas, 2000: Low-level atmospheric jets and inversions over the western Weddell Sea. *Bound.-Layer Meteor.*, **97**, 459–486, doi:10.1023/A:1002793831076.

Arritt, R. W., T. D. Rink, M. Segal, D. P. Todey, C. A. Clark, M. J. Mitchell, and K. M. Labas, 1997: The Great Plains low-level jet during the warm season of 1993. *Mon. Wea. Rev.*, **125**, 2176–2192, doi:10.1175/1520-0493(1997)125<2176:TGPLLJ>2.0.CO;2.

Axelsen, S. L., and H. van Dop, 2009: Large-eddy simulation of katabatic winds. Part 2: Sensitivity study and comparison with analytical models. *Acta Geophys.*, **57**, 837–856, doi:10.2478/s11600-009-0042-5.

Baas, P., F. C. Bosveld, H. Klein Baltink, and A. A. M. Holtslag, 2009: A climatology of nocturnal low-level jets at Cabauw. *J. Appl. Meteor. Climatol.*, **48**, 1627–1642, doi:10.1175/2009JAMC1965.1.

Banta, R. M., 2008: Stable-boundary-layer regimes from the perspective of the low-level jet. *Acta Geophys.*, **56**, 58–87, doi:10.2478/s11600-007-0049-8.

——, and Coauthors, 1998: Daytime buildup and nighttime transport of urban ozone in the boundary layer during a stagnation episode. *J. Geophys. Res.*, **103**, 22 519–22 544, doi:10.1029/98JD01020.

——, R. K. Newsom, J. K. Lundquist, Y. L. Pichugina, R. L. Coulter, and L. Mahrt, 2002: Nocturnal low-level jet characteristics over Kansas during CASES-99. *Bound.-Layer Meteor.*, **105**, 221–252, doi:10.1023/A:1019992330866.

——, Y. L. Pichugina, N. D. Kelley, R. M. Hardesty, and W. A. Brewer, 2013: Wind energy meteorology: Insight into wind properties in the turbine-rotor layer of the atmosphere from high-resolution Doppler lidar. *Bull. Amer. Meteor. Soc.*, **94**, 883–902, doi:10.1175/BAMS-D-11-00057.1.

Bao, J. W., S. A. Michelson, P. O. G. Persson, I. V. Djalalova, and J. M. Wilczak, 2008: Observed and WRF-simulated low-level winds in a high-ozone episode during the Central California Ozone Study. *J. Appl. Meteor. Climatol.*, **47**, 2372–2394, doi:10.1175/2008JAMC1822.1.

Beyrich, F., D. Kalass, and U. Weisensee, 1997: Influence of the nocturnal low-level jet on the vertical and mesoscale structure of the stable boundary layer as revealed from Doppler-sodar-observations. *Acoustic Remote Sensing Applications*, S. P. Singal, Ed., Narosa Publishing House, 236–246.

Blackadar, A. K., 1957: Boundary layer wind maxima and their significance for the growth of nocturnal inversions. *Bull. Amer. Meteor. Soc.*, **38**, 283–290.

Bonner, W. D., 1968: Climatology of the low level jet. *Mon. Wea. Rev.*, **96**, 833–850, doi:10.1175/1520-0493(1968)096<0833:COTLLJ>2.0.CO;2.

——, and J. Paegle, 1970: Diurnal variations in boundary layer winds over the south-central United States in summer. *Mon. Wea. Rev.*, **98**, 735–744, doi:10.1175/1520-0493(1970)098<0735:DVIBLW>2.3.CO;2.

——, S. Esbensen, and R. Greenberg, 1968: Kinematics of the low-level jet. *J. Appl. Meteor.*, **7**, 339–347, doi:10.1175/1520-0450(1968)007<0339:KOTLLJ>2.0.CO;2.

Brook, R. R., 1985: The Koorin nocturnal low-level jet. *Bound.-Layer Meteor.*, **32**, 133–154, doi:10.1007/BF00120932.

Brown, R. A., 1974: *Analytical Methods in Planetary Boundary-Layer Modelling*. Wiley, 148 pp.

Buajitti, K., and A. K. Blackadar, 1957: Theoretical studies of diurnal wind-structure variations in the planetary boundary layer. *Quart. J. Roy. Meteor. Soc.*, **83**, 486–500, doi:10.1002/qj.49708335804.

Businger, J. A., J. C. Wyngaard, Y. Izumi, and E. F. Bradley, 1971: Flux-profile relationships in the atmospheric surface layer. *J. Atmos. Sci.*, **28**, 181–189, doi:10.1175/1520-0469(1971)028<0181:FPRITA>2.0.CO;2.

Carslaw, H. S., and J. C. Jaeger, 1959: *Conduction of Heat in Solids*. 2nd ed. Clarendon Press, 510 pp.

Conangla, L., and J. Cuxart, 2006: On the turbulence in the upper part of the low-level jet: An experimental and numerical study. *Bound.-Layer Meteor.*, **118**, 379–400, doi:10.1007/s10546-005-0608-y.

Cosack, N., S. Emeis, and M. Kühn, 2007: On the influence of low-level jets on energy production and loading of wind turbines. *Wind Energy: Proceedings of the Euromech Colloquium*, J. Peinke, I. P. Schaumann, and S. Barth, Eds., Springer, 325–328, doi:10.1007/978-3-540-33866-6_61.

Cotton, W. R., M. S. Lin, R. L. McAnelly, and C. J. Tremback, 1989: A composite model of mesoscale convective complexes. *Mon. Wea. Rev.*, **117**, 765–783, doi:10.1175/1520-0493(1989)117<0765:ACMOMC>2.0.CO;2.

Coulter, R. L., 1981: Nocturnal wind profile characteristics. *Proc. First Int. Symp. on Acoustic Remote Sensing of the Atmosphere and Oceans*, Calgary, AB, Canada, University of Calgary, 6.1–6.11.

Cuxart, J., and M. A. Jiménez, 2007: Mixing processes in a nocturnal low-level jet: An LES study. *J. Atmos. Sci.*, **64**, 1666–1679, doi:10.1175/JAS3903.1.

Darby, L. S., K. J. Allwine, and R. M. Banta, 2006: Nocturnal low-level jet in a mountain basin complex. Part II: Transport and diffusion of tracer under stable conditions. *J. Appl. Meteor. Climatol.*, **45**, 740–753, doi:10.1175/JAM2367.1.

Delgado, R., S. D. Rabenhorst, B. B. Demoz, and R. M. Huff, 2014: Elastic lidar measurements of summer nocturnal low level jet events over Baltimore, Maryland. *J. Atmos. Chem.*, **72**, 311–333, doi:10.1007/s10874-013-9277-2.

Derbyshire, S. H., 1999: Stable boundary-layer modelling: Established approaches and beyond. *Bound.-Layer Meteor.*, **90**, 423–446, doi:10.1023/A:1001749007836.

Drake, V. A., and R. A. Farrow, 1988: The influence of atmospheric structure and motions on insect migration. *Annu. Rev. Entomol.*, **33**, 183–210, doi:10.1146/annurev.en.33.010188.001151.

Du, Y., and R. Rotunno, 2014: A simple analytical model of the nocturnal low-level jet over the Great Plains of the United States. *J. Atmos. Sci.*, **71**, 3674–3683, doi:10.1175/JAS-D-14-0060.1.

Egger, J., 1985: Slope winds and the axisymmetric circulation over Antarctica. *J. Atmos. Sci.*, **42**, 1859–1867, doi:10.1175/1520-0469(1985)042<1859:SWATAC>2.0.CO;2.

Emeis, S., 2013: *Wind Energy Meteorology: Atmospheric Physics for Wind Power Generation*. Springer, 196 pp., doi:10.1007/978-3-642-30523-8.

——, 2014: Current issues in wind energy meteorology. *Meteor. Appl.*, **21**, 803–819, doi:10.1002/met.1472.

Fernando, H. J. S., and J. C. Weil, 2010: Whither the stable boundary layer? *Bull. Amer. Meteor. Soc.*, **91**, 1475–1484, doi:10.1175/2010BAMS2770.1.

Fiedler, S., K. Schepanski, B. Heinold, P. Knippertz, and I. Tegen, 2013: Climatology of nocturnal low-level jets over North Africa and implications for modeling mineral dust emission. *J. Geophys. Res. Atmos.*, **118**, 6100–6121, doi:10.1002/jgrd.50394.

French, A. J., and M. D. Parker, 2010: The response of simulated nocturnal convective systems to a developing low-level jet. *J. Atmos. Sci.*, **67**, 3384–3408, doi:10.1175/2010JAS3329.1.

Garrett, C., 1991: Marginal mixing theories. *Atmos.–Ocean*, **29**, 313–339, doi:10.1080/07055900.1991.9649407.

——, P. MacCready, and P. Rhines, 1993: Boundary mixing and arrested Ekman layers: Rotating stratified flow near a sloping boundary. *Annu. Rev. Fluid Mech.*, **25**, 291–323, doi:10.1146/annurev.fl.25.010193.001451.

Gibson, M. M., and B. E. Launder, 1978: Ground effects on pressure fluctuations in the atmospheric boundary layer. *J. Fluid Mech.*, **86**, 491–511, doi:10.1017/S0022112078001251.

Grisogono, B., 1995: A generalized Ekman layer profile with gradually varying eddy diffusivities. *Quart. J. Roy. Meteor. Soc.*, **121**, 445–453, doi:10.1002/qj.49712152211.

Gutman, L. N., and V. M. Malbakhov, 1964: On the theory of katabatic winds of Antarctic (in Russian). *Meteor. Issled.*, **9**, 150–155.

Higgins, R. W., Y. Yao, E. S. Yaresh, J. E. Janowiak, and K. C. Mo, 1997: Influence of the Great Plains low-level jet on summertime precipitation and moisture transport over the central United States. *J. Climate*, **10**, 481–507, doi:10.1175/1520-0442(1997)010<0481:IOTGPL>2.0.CO;2.

Hoecker, W. H., 1963: Three southerly low-level jet systems delineated by the Weather Bureau special pibal network of 1961. *Mon. Wea. Rev.*, **91**, 573–582, doi:10.1175/1520-0493(1963)091<0573:TSLJSD>2.3.CO;2.

Holton, J. R., 1967: The diurnal boundary layer wind oscillation above sloping terrain. *Tellus*, **19A**, 199–205, doi:10.1111/j.2153-3490.1967.tb01473.x.

Holtslag, A. A. M., and Coauthors, 2013: Stable atmospheric boundary layers and diurnal cycles: Challenges for weather and climate models. *Bull. Amer. Meteor. Soc.*, **94**, 1691–1706, doi:10.1175/BAMS-D-11-00187.1.

Howell, J. F., and J. Sun, 1999: Surface-layer fluxes in stable conditions. *Bound.-Layer Meteor.*, **90**, 495–520, doi:10.1023/A:1001788515355.

Hu, X.-M., P. M. Klein, M. Xue, J. K. Lundquist, F. Zhang, and Y. Qi, 2013: Impact of low-level jets on the nocturnal urban heat island intensity in Oklahoma City. *J. Appl. Meteor. Climatol.*, **52**, 1779–1802, doi:10.1175/JAMC-D-12-0256.1.

Isard, S. A., and S. H. Gage, 2001: *Flow of Life in the Atmosphere: An Airscape Approach to Understanding Invasive Organisms*. Michigan State University Press, 240 pp.

Jeffrey, D. J., and A. C. Norman, 2004: Not seeing the roots for the branches: Multivalued functions in computer algebra. *ACM SIGSAM Bull.*, **38**, 57–66, doi:10.1145/1040034.1040036.

Jeričević, A., and Ž. Večenaj, 2009: Improvement of vertical diffusion analytic schemes under stable atmospheric conditions. *Bound.-Layer Meteor.*, **131**, 293–307, doi:10.1007/s10546-009-9367-5.

Jiang, X., N.-C. Lau, I. M. Held, and J. J. Ploshay, 2007: Mechanisms of the Great Plains low-level jet as simulated in an AGCM. *J. Atmos. Sci.*, **64**, 532–547, doi:10.1175/JAS3847.1.

Kallistratova, M. A., and R. D. Kouznetsov, 2012: Low-level jets in the Moscow region in summer and winter observed with a sodar network. *Bound.-Layer Meteor.*, **143**, 159–175, doi:10.1007/s10546-011-9639-8.

Klein, P. M., X.-M. Hu, and M. Xue, 2014: Impacts of mixing processes in nocturnal atmospheric boundary layer on urban

ozone concentrations. *Bound.-Layer Meteor.*, **150**, 107–130, doi:10.1007/s10546-013-9864-4.

Kuo, H. L., 1973: On a simplified radiative-conductive heat transfer equation. *Pure Appl. Geophys.*, **109**, 1870–1876, doi:10.1007/BF00876111.

Lykosov, V. N., and L. N. Gutman, 1972: Turbulent boundary layer above a sloping underlying surface. *Izv. Atmos. Oceanic Phys.*, **8**, 799–809.

MacCready, P., and P. B. Rhines, 1991: Buoyant inhibition of Ekman transport on a slope and its effect on stratified spin-up. *J. Fluid Mech.*, **223**, 631–661, doi:10.1017/S0022112091001581.

——, and ——, 1993: Slippery bottom boundary layers on a slope. *J. Phys. Oceanogr.*, **23**, 5–22, doi:10.1175/1520-0485(1993)023<0005:SBBLOA>2.0.CO;2.

Maddox, R. A., 1980: Mesoscale convective complexes. *Bull. Amer. Meteor. Soc.*, **61**, 1374–1387, doi:10.1175/1520-0477(1980)061<1374:MCC>2.0.CO;2.

——, 1983: Large-scale meteorological conditions associated with midlatitude mesoscale convective complexes. *Mon. Wea. Rev.*, **111**, 1475–1493, doi:10.1175/1520-0493(1983)111<1475:LSMCAW>2.0.CO;2.

Mahrt, L., 1982: Momentum balance of gravity flows. *J. Atmos. Sci.*, **39**, 2701–2711, doi:10.1175/1520-0469(1982)039<2701:MBOGF>2.0.CO;2.

——, 1998: Stratified atmospheric boundary layers and breakdown of models. *Theor. Comput. Fluid Dyn.*, **11**, 263–279, doi:10.1007/s001620050093.

——, 1999: Stratified atmospheric boundary layers. *Bound.-Layer Meteor.*, **90**, 375–396, doi:10.1023/A:1001765727956.

——, R. C. Heald, D. H. Lenschow, B. B. Stankov, and I. Troen, 1979: An observational study of the structure of the nocturnal boundary layer. *Bound.-Layer Meteor.*, **17**, 247–264, doi:10.1007/BF00117983.

Mao, H., and R. Talbot, 2004: Role of meteorological processes in two New England ozone episodes during summer 2001. *J. Geophys. Res.*, **109**, D20305, doi:10.1029/2004JD004850.

McNider, R. T., and R. A. Pielke, 1981: Diurnal boundary-layer development over sloping terrain. *J. Atmos. Sci.*, **38**, 2198–2212, doi:10.1175/1520-0469(1981)038<2198:DBLDOS>2.0.CO;2.

Means, L. L., 1954: A study of the mean southerly wind maximum in low levels associated with a period of summer precipitation in the middle west. *Bull. Amer. Meteor. Soc.*, **35**, 166–170.

Miles, J., 1994: Analytical solutions for the Ekman layer. *Bound.-Layer Meteor.*, **67**, 1–10, doi:10.1007/BF00705505.

Milionis, A. E., and T. D. Davies, 2002: Associations between atmospheric temperature inversions and vertical wind profiles: A preliminary assessment. *Meteor. Appl.*, **9**, 223–228, doi:10.1017/S1350482702002074.

Mirocha, J. D., M. D. Simpson, J. D. Fast, L. K. Berg, and R. L. Baskett, 2016: Investigation of boundary-layer wind predictions during nocturnal low-level jet events using the Weather Research and Forecasting model. *Wind Energy*, **19**, 739–762, doi:10.1002/we.1862.

Mironov, D., and E. Fedorovich, 2010: On the limiting effect of the Earth's rotation on the depth of a stably stratified boundary layer. *Quart. J. Roy. Meteor. Soc.*, **136**, 1473–1480, doi:10.1002/qj.631.

Mitchell, M. J., R. W. Arritt, and K. Labas, 1995: A climatology of the warm season Great Plains low-level jet using wind profiler observations. *Wea. Forecasting*, **10**, 576–591, doi:10.1175/1520-0434(1995)010<0576:ACOTWS>2.0.CO;2.

Mo, R., 2013: On adding thermodynamic damping mechanisms to refine two classical models of katabatic winds. *J. Atmos. Sci.*, **70**, 2325–2334, doi:10.1175/JAS-D-12-0256.1.

Nieuwstadt, F. T. M., 1983: On the solution of the stationary, baroclinic Ekman-layer equations with a finite boundary-layer height. *Bound.-Layer Meteor.*, **26**, 377–390, doi:10.1007/BF00119534.

O'Brien, J. J., 1970: A note on the vertical structure of the eddy exchange coefficient in the planetary boundary layer. *J. Atmos. Sci.*, **27**, 1213–1215, doi:10.1175/1520-0469(1970)027<1213:ANOTVS>2.0.CO;2.

Paegle, J., and G. E. Rasch, 1973: Three-dimensional characteristics of diurnally varying boundary-layer flows. *Mon. Wea. Rev.*, **101**, 746–756, doi:10.1175/1520-0493(1973)101<0746:TCODVB>2.3.CO;2.

Pan, Z., M. Segal, and R. W. Arritt, 2004: Role of topography in forcing low-level jets in the central United States during the 1993 flood-altered terrain simulations. *Mon. Wea. Rev.*, **132**, 396–403, doi:10.1175/1520-0493(2004)132<0396:ROTIFL>2.0.CO;2.

Parish, T. R., and L. D. Oolman, 2010: On the role of sloping terrain in the forcing of the Great Plains low-level jet. *J. Atmos. Sci.*, **67**, 2690–2699, doi:10.1175/2010JAS3368.1.

Pitchford, K. L., and J. London, 1962: The low-level jet as related to nocturnal thunderstorms over the Midwest United States. *J. Appl. Meteor.*, **1**, 43–47, doi:10.1175/1520-0450(1962)001<0043:TLLJAR>2.0.CO;2.

Pu, B., and R. Dickinson, 2014: Diurnal spatial variability of Great Plains summer precipitation related to the dynamics of the low-level jet. *J. Atmos. Sci.*, **71**, 1807–1817, doi:10.1175/JAS-D-13-0243.1.

Reicosky, D. C., L. J. Winkelman, J. M. Baker, and D. G. Baker, 1989: Accuracy of hourly air temperatures calculated from daily minima and maxima. *Agric. For. Meteor.*, **46**, 193–209, doi:10.1016/0168-1923(89)90064-6.

Rife, D. L., J. O. Pinto, A. J. Monaghan, C. A. Davis, and J. R. Hannan, 2010: Global distribution and characteristics of diurnally varying low-level jets. *J. Climate*, **23**, 5041–5064, doi:10.1175/2010JCLI3514.1.

Sadler, E. J., and R. E. Schroll, 1997: An empirical model of diurnal temperature patterns. *Agron. J.*, **89**, 542–548, doi:10.2134/agronj1997.00021962008900040002x.

Sanders, C. G., 1975: Comments on the model for estimating the completion of rest for "Red Haven" and "Elberta" peach trees. *Hortic. Sci.*, **10**, 560–561.

Sandu, I., A. Beljaars, P. Bechtold, T. Mauritsen, and G. Balsamo, 2013: Why is it so difficult to represent stably stratified conditions in numerical weather prediction (NWP) models? *J. Adv. Model. Earth Syst.*, **5**, 117–133, doi:10.1002/jame.20013.

Sangster, W. E., 1967: Diurnal surface geostrophic wind variations over the Great Plains. Preprints, *Fifth Conf. on Severe Local Storms*, St. Louis, MO, Amer. Meteor. Soc., 146–153.

Savijärvi, H., 1991: The United States Great Plains diurnal ABL variation and the nocturnal low-level jet. *Mon. Wea. Rev.*, **119**, 833–840, doi:10.1175/1520-0493(1991)119<0833:TUSGPD>2.0.CO;2.

Schumann, U., and T. Gerz, 1995: Turbulent mixing in stably stratified shear flows. *J. Appl. Meteor.*, **34**, 33–48, doi:10.1175/1520-0450-34.1.33.

Shapiro, A., and E. Fedorovich, 2008: Coriolis effects in homogeneous and inhomogeneous katabatic flows. *Quart. J. Roy. Meteor. Soc.*, **134**, 353–370, doi:10.1002/qj.217.

——, and ——, 2009: Nocturnal low-level jet over a shallow slope. *Acta Geophys.*, **57**, 950–980, doi:10.2478/s11600-009-0026-5.

——, and ——, 2010: Analytical description of a nocturnal low-level jet. *Quart. J. Roy. Meteor. Soc.*, **136**, 1255–1262, doi:10.1002/qj.628.

——, and ——, 2013: Similarity models for unsteady free convection flows along a differentially cooled horizontal surface. *J. Fluid Mech.*, **736**, 444–463, doi:10.1017/jfm.2013.538.

Sheih, C. M., 1972: A theoretical study of the diurnal wind variations in the planetary boundary layer. *J. Atmos. Sci.*, **29**, 995–998, doi:10.1175/1520-0469(1972)029<0995:ATSOTD>2.0.CO;2.

Singh, M. P., R. T. McNider, and J. T. Lin, 1993: An analytical study of diurnal wind-structure variations in the boundary layer and the low-level nocturnal jet. *Bound.-Layer Meteor.*, **63**, 397–423, doi:10.1007/BF00705360.

Sládkovič, R., and H.-J. Kanter, 1977: Low-level jet in the Bavarian pre-alpine region. *Arch. Meteor. Geophys. Bioklimatol.*, **25A**, 343–355.

Solomon, P., E. Cowling, G. Hidy, and C. Furiness, 2000: Comparison of scientific findings from major ozone field studies in North America and Europe. *Atmos. Environ.*, **34**, 1885–1920, doi:10.1016/S1352-2310(99)00453-7.

Song, J., K. Liao, R. L. Coulter, and B. M. Lesht, 2005: Climatology of the low-level jet at the Southern Great Plains Atmospheric Boundary Layer Experiments site. *J. Appl. Meteor.*, **44**, 1593–1606, doi:10.1175/JAM2294.1.

Steeneveld, G. J., 2014: Current challenges in understanding and forecasting stable boundary layers over land and ice. *Front. Environ. Sci.*, **2**, 41, doi:10.3389/fenvs.2014.00041.

——, T. Mauritsen, E. I. F. de Bruijn, J. Vilà-Guerau de Arellano, G. Svensson, and A. A. M. Holtslag, 2008: Evaluation of limited-area models for the representation of the diurnal cycle and contrasting nights in CASES-99. *J. Appl. Meteor. Climatol.*, **47**, 869–887, doi:10.1175/2007JAMC1702.1.

Stensrud, D. J., 1996: Importance of low-level jets to climate: A review. *J. Climate*, **9**, 1698–1711, doi:10.1175/1520-0442(1996)009<1698:IOLLJT>2.0.CO;2.

Stiperski, I., I. Kavčič, B. Grisogono, and D. R. Durran, 2007: Including Coriolis effects in the Prandtl model for katabatic flow. *Quart. J. Roy. Meteor. Soc.*, **133**, 101–106, doi:10.1002/qj.19.

Storm, B., J. Dudhia, S. Basu, A. Swift, and I. Giammanco, 2009: Evaluation of the Weather Research and Forecasting model on forecasting low-level jets: Implications for wind energy. *Wind Energy*, **12**, 81–90, doi:10.1002/we.288.

Stull, R. B., 1988: *An Introduction to Boundary Layer Meteorology*. Kluwer, 666 pp.

Tan, Z.-M., 2001: An approximate analytical solution for the baroclinic and variable eddy diffusivity semi-geostrophic Ekman boundary layer. *Bound.-Layer Meteor.*, **98**, 361–385, doi:10.1023/A:1018708726112.

——, and M. M. Farahani, 1998: An analytical study of the diurnal variations of wind in a semi-geostrophic Ekman boundary layer model. *Bound.-Layer Meteor.*, **86**, 313–332, doi:10.1023/A:1000694732459.

Thorpe, A. J., and T. H. Guymer, 1977: The nocturnal jet. *Quart. J. Roy. Meteor. Soc.*, **103**, 633–653, doi:10.1002/qj.49710343809.

Ting, M., and H. Wang, 2006: The role of the North American topography on the maintenance of the Great Plains summer low-level jet. *J. Atmos. Sci.*, **63**, 1056–1068, doi:10.1175/JAS3664.1.

Trier, S. B., C. A. Davis, D. A. Ahijevych, M. L. Weisman, and G. H. Bryan, 2006: Mechanisms supporting long-lived episodes of propagating nocturnal convection within a 7-day WRF Model simulation. *J. Atmos. Sci.*, **63**, 2437–2461, doi:10.1175/JAS3768.1.

——, ——, and R. E. Carbone, 2014: Mechanisms governing the persistence and diurnal cycle of a heavy rainfall corridor. *J. Atmos. Sci.*, **71**, 4102–4126, doi:10.1175/JAS-D-14-0134.1.

U.S. Naval Observatory, 2016: Sun or moon rise/set table for one year. Astronomical Applications Department. Subset used: 2008, accessed 21 February 2016. [Available online at http://aa.usno.navy.mil/data/docs/RS_OneYear.php.]

Van de Wiel, B. J. H., A. F. Moene, G. J. Steeneveld, P. Baas, F. C. Bosveld, and A. A. M. Holtslag, 2010: A conceptual view on inertial oscillations and nocturnal low-level jets. *J. Atmos. Sci.*, **67**, 2679–2689, doi:10.1175/2010JAS3289.1.

Walters, C. K., J. A. Winkler, R. P. Shadbolt, J. van Ravensway, and G. D. Bierly, 2008: A long-term climatology of southerly and northerly low-level jets for the central United States. *Ann. Assoc. Amer. Geogr.*, **98**, 521–552, doi:10.1080/00045600802046387.

——, ——, S. Husseini, R. Keeling, J. Nikolic, and S. Zhong, 2014: Low-level jets in the North American Regional Reanalysis (NARR): A comparison with rawinsonde observations. *J. Appl. Meteor. Climatol.*, **53**, 2093–2113, doi:10.1175/JAMC-D-13-0364.1.

Werth, D., R. Kurzeja, N. L. Dias, G. Zhang, H. Duarte, M. Fischer, M. Parker, and M. Leclerc, 2011: The simulation of the southern Great Plains nocturnal boundary layer and the low-level jet with a high-resolution mesoscale atmospheric model. *J. Appl. Meteor. Climatol.*, **50**, 1497–1513, doi:10.1175/2011JAMC2272.1.

Westbrook, J. K., 2008: Noctuid migration in Texas within the nocturnal aeroecological boundary layer. *Integr. Comp. Biol.*, **48**, 99–106, doi:10.1093/icb/icn040.

——, and S. A. Isard, 1999: Atmospheric scales of biotic dispersal. *Agric. For. Meteor.*, **97**, 263–274, doi:10.1016/S0168-1923(99)00071-4.

Wexler, H., 1961: A boundary layer interpretation of the low-level jet. *Tellus*, **13A**, 368–378, doi:10.1111/j.2153-3490.1961.tb00098.x.

Whiteman, C. D., X. Bian, and S. Zhong, 1997: Low-level jet climatology from enhanced rawinsonde observations at a site in the southern Great Plains. *J. Appl. Meteor.*, **36**, 1363–1376, doi:10.1175/1520-0450(1997)036<1363:LLJCFE>2.0.CO;2.

Wilson, J. D., 2012: An alternative eddy-viscosity model for the horizontally uniform atmospheric boundary layer. *Bound.-Layer Meteor.*, **145**, 165–184, doi:10.1007/s10546-011-9650-0.

Wolf, W. W., J. K. Westbrook, J. Raulston, S. D. Pair, and S. E. Hobbs, 1990: Recent airborne radar observations of migrant pests in the United States. *Philos. Trans. Roy. Soc. London*, **B328**, 619–630, doi:10.1098/rstb.1990.0132.

Zhong, S., J. D. Fast, and X. Bian, 1996: A case study of the Great Plains low-level jet using wind profiler network data and a high-resolution mesoscale model. *Mon. Wea. Rev.*, **124**, 785–806, doi:10.1175/1520-0493(1996)124<0785:ACSOTG>2.0.CO;2.

Zhu, M., E. B. Radcliffe, D. W. Ragsdale, I. V. MacRae, and M. W. Seeley, 2006: Low-level jet streams associated with spring aphid migration and current season spread of potato viruses in the U.S. northern Great Plains. *Agric. For. Meteor.*, **138**, 192–202, doi:10.1016/j.agrformet.2006.05.001.

Zunckel, M., G. Held, R. A. Preston-Whyte, and A. Joubert, 1996: Low-level wind maxima and the transport of pyrogenic products over southern Africa. *J. Geophys. Res.*, **101**, 23 745–23 755, doi:10.1029/95JD02602.